Electronic Supplementary Information for:

Ultrafast Electron Transfer from Higher Excited States in Perylene Monoimide–Nanocrystal Hybrids Revealed by Pump-Push-Probe Spectroscopy

Mizuki Sato,[1] Daisuke Yoshioka,[1] Hikaru Sotome,[2] Yuki Nagai,[1] and Yoichi Kobayashi[1,]*

[1]*Department of Applied Chemistry, College of Life Sciences, Ritsumeikan University, Kusatsu, Shiga, Japan.*

[2]*Division of Frontier Materials Science and Center for Advanced Interdisciplinary Research, Graduate School of Engineering Science, The University of Osaka, Osaka, Japan*

Corresponding Author
*ykobayas@fc.ritsumei.ac.jp

CONTENTS

1. Experimental setup

Materials

3,4,9,10-Perylenetetracarboxylic dianhydride, imidazole, chlorobenzene, bromine, 1-octadecene, ethyl 4-(4,4,5,5-tetramethyl-1,3,2-dioxaborolan-2-yl)benzoate, tetrabutylammonium, rhodamine 6G, potassium carbonate (K_2CO_3), tetrakis(triphenylphosphine)palladium(0) ($Pd(PPh_3)_4$), hexafluorophosphate ($TBAPF_6$), and cadmium oxide (CdO) were purchased from Tokyo Chemical Industry. Zinc acetate dihydrate ($Zn(OAc)_2 \cdot H_2O$), sodium sulfate (Na_2SO_4), potassium hydroxide (KOH), sodium thiosulfate, sulfur, zinc stearate, oleylamine and oleic acid were purchased from Wako Co. Ltd. 2,6-Diisopropylaniline was purchased from Sigma-Aldrich Co. LLC. Chloroform ($CHCl_3$), hexane, toluene, dichloromethane, tetrahydrofuran (THF), hydrochloric acid (HCl), methanol, acetone, ethyl acetate, diethyl ether, ethanol, acetonitrile, chloroform-d_1, 99.8 atom % D with 0.03vol% TMS ($CDCl_3$) and silica gel 60N were purchased from Kanto Chemical Co., Inc.

Setups for material characterization and steady-state optical measurements

Characterization of the organic molecules

All reactions were monitored by thin-layer chromatography carried out on 0.2 mm E. Merck silica gel plates (60F-254). The ^1H and ^{13}C NMR spectra were recorded at 500 MHz and 126 MHz on a JNM-ECS500 (JEOL), respectively. High performance liquid chromatography (HPLC) was conducted with a Chromaster (Hitachi High-Technologies) equipped with a normal-phase analytical column (Mightysil RP-18GP II, 25 cm × 4.6 mm, 5 μm particle, Kanto Chemical Co., Inc.) and a linear photodiode array (PDA) detector. Gel permeation chromatography (GPC) was conducted with a recycling preparative HPLC series (Japan Analytical Industry Co., Ltd.) equipped with two GPC columns (JAIGEL-2HR Plus) and a UV detector. $CHCl_3$ was used as an eluent with the flow rate of 10 mL/min. Cyclic voltammetry was carried out using a potentiostat analyzer (EC FRONTIER, ECstat-301) with a three-electrode cell consisting of a glassy carbon disk working electrode (0.6 cm in diameter), an Ag/Ag^+ reference electrode, and a platinum wire counter electrode.

Characterization of the nanocrystals

Nanocrystals (NCs) were purified by centrifugation using a low-speed centrifuge (TOMY, LCX-100) equipped with an angle rotor (TOMY, CA-16) for eight 50 mL conical tubes (maximum radius 105 mm, minimum radius 42 mm, tube angle = 25°, maximum speed = 10,000 rpm). X-ray diffraction (XRD) patterns were recorded in an X-ray diffractometer (Rigaku Ultima IV) with Cu Kα radiation (λ = 1.5406 Å). The size and shape of NCs were analyzed by a transmission electron microscope (TEM, JEOL JEM-2100plus).

Basic optical properties

Steady-state absorption spectra were measured with UV-3600 (Shimadzu), using a 10-mm quartz cuvette in air. The steady-state fluorescence spectra were measured using an RF-6000 (SHIMADZU) with a 10-mm quartz cuvette under a nitrogen atmosphere.

Setup for pump-probe spectroscopy

Transient absorption measurements on the subpicosecond to nanosecond timescale were conducted by a homemade pump−probe system.[1] Specifically, an amplified femtosecond laser, Spirit One 1040-8 (Spectra-Physics, 1040-nm, the pulse width: ∼270 fs), was split into two beams with a ratio of 1:9. The stronger beam was directed to a noncollinear optical parametric amplifier (NOPA), Spirit-NOPA-3H (Spectra-Physics), to generate the 520-nm femtosecond laser pulse for the pump beam. The pump beam was chopped before the sample at 500 Hz for signal differencing. The other weaker beam was focused on deuterated water placed in a 10-mm quartz cuvette to generate the white light continuum for the probe beam. Both pump and probe beams were focused on the sample solution placed in the 2-mm quartz cuvette. The relative polarization between the pump and probe pulses was set to the magic angle. The transmitted probe beam was detected with a multichannel detection system, PK120-C-RK (UNISOKU), composed of a CMOS linear image sensor and a polychromator. The obtained spectra were calibrated for group velocity dispersion using the data obtained from the optical Kerr signal of $CHCl_3$ between the pump pulse and the white-light continuum. The instrumental response function was approximately 100 fs. All measurements were performed at room temperature; sample solutions were purged with N2 gas for 10 min prior to measurement.

Setup for pump-push-probe spectroscopy

The setup is similar to that of the pump-probe measurement, except for the excitation pulses. A 650-nm push pulse was generated by NOPA and used as the second excitation pulse. A residual 520-nm pulse from an auxiliary output port of the NOPA was used as the first pump pulse. The time delay between the two pulses was controlled by a manual linear translation stage.

2. Synthesis of materials

Scheme S1. Synthesis of PMI.

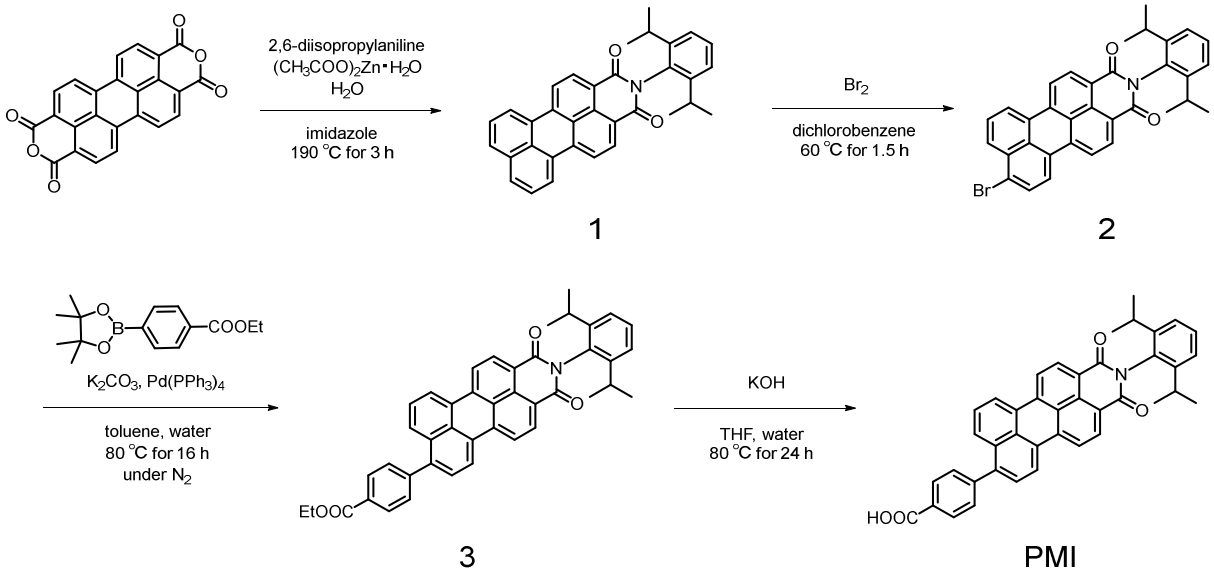

Synthesis of compound 1[2]

3,4,9,10-Perylene tetracarboxylic dianhydride (200 mg, 0.510 mmol), $Zn(OAc)_2 \cdot H_2O$ (112 mg, 0.510 mmol), imidazole (2.50 g), 2,6-diisopropylaniline (140 mg, 0.790 mmol), and water (18 mL) were placed in a microwave reaction vessel. The mixture was heated under microwave irradiation at 190 °C and 80 W for 3 h. After cooling to room temperature, the reaction mixture was dissolved in dichloromethane (150 mL), and water (150 mL) was added. The resulting biphasic mixture was filtered and separated. The organic phase was washed with 1 M HCl aqueous solution (60 mL × 2) and then with water (60 mL). The organic layer was dried over anhydrous Na_2SO_4, filtered, and concentrated under reduced pressure. The crude product was purified by column chromatography on silica gel using $CHCl_3$/hexane (v/v = 4:1) as the eluent to afford a red solid (75.6 mg, 30.8%).

^{1}H NMR (500 MHz, $CDCl_3$) δ 8.68 (d, J = 8.0 Hz, 2H), 8.51 (t, J = 8.6 Hz, 4H), 7.95 (d, J = 7.4 Hz, 2H), 7.68 (t, J = 7.7 Hz, 2H), 7.48 (t, J = 7.4 Hz, 1H), 7.34 (d, J = 7.4 Hz, 2H), 2.75 (q, J = 6.7 Hz, 2H), 1.17 (d, J = 6.9 Hz, 12H).

Synthesis of compound 2[3]

Compound **1** (100 mg, 0.208 mmol) was dissolved in chlorobenzene (10 mL) with moderate heating. Bromine (434 mg, 2.72 mmol) was added to the solution, and the reaction mixture was stirred at 60 °C for 1.5 h under a nitrogen atmosphere. After completion of the reaction, excess bromine was removed by purging with a nitrogen flow, and an aqueous solution of sodium thiosulfate (2 M, 50 mL) was added to quench the reaction. The solvent was removed under reduced pressure, and the crude product was purified by column chromatography on silica gel using $CHCl_3$/toluene (v/v = 1:1) as the eluent to afford a red solid (112 mg, 95.1%).

^{1}H NMR (500 MHz, $CDCl_3$) δ 8.67 (dd, J = 8.0, 6.3 Hz, 2H), 8.55 (d, J = 7.4 Hz, 1H), 8.51 (d, J = 8.0 Hz, 1H), 8.47 (d, J = 8.0 Hz, 1H), 8.36 (d, J = 8.0 Hz, 1H), 8.31 (d, J = 8.6 Hz, 1H), 7.96 (d, J = 8.6 Hz, 1H), 7.77 (t, J = 8.0 Hz, 1H), 7.47 (t, J = 8.0 Hz, 1H), 7.33 (d, J = 7.4 Hz, 2H), 2.77–2.71 (m, 2H), 1.17 (t, J = 6.3 Hz, 12H).

Synthesis of compound 3[4]

Compound **2** (128 mg, 0.228 mmol), ethyl 4-(4,4,5,5-tetramethyl-1,3,2-dioxaborolan-2-yl)benzoate (178 mg, 0.645 mmol), toluene (35 mL), and an aqueous solution of K_2CO_3 (2 M, 10 mL) were placed in a round-bottom flask. The mixture was purged with nitrogen for 15 min, after which $Pd(PPh_3)_4$ (73.1 mg, 0.0633 mmol) was added. The reaction mixture was stirred at 80 °C for 16 h under a nitrogen atmosphere. After cooling to room temperature, the reaction mixture was filtered and the phases were separated. The organic layer was washed twice with water (2 × 60 mL), dried over anhydrous Na_2SO_4, filtered, and the solvent was removed under reduced pressure. The crude product was purified by column chromatography on silica gel using dichloromethane/hexane (v/v = 7:2) as the eluent to afford a red solid (108 mg, 74.5%).

^{1}H NMR (500 MHz, $CDCl_3$) δ 8.70 (dd, J = 8.0, 1.7 Hz, 2H), 8.57–8.52 (m, 4H), 8.24 (d, J = 8.0 Hz, 2H), 7.96 (d, J = 8.0 Hz, 1H), 7.65–7.62 (m, 4H), 7.49 (t, J = 7.7 Hz, 1H), 7.35 (d, J = 8.0 Hz, 2H), 4.46 (q, J = 7.1 Hz, 2H), 2.80–2.75 (m, 2H), 1.46 (t, J = 7.2 Hz, 3H), 1.18 (d, J = 6.9 Hz, 12H).

Synthesis of PMI[4]

An aqueous solution of KOH (2 M, 20 mL) was added to a solution of compound **3** (108 mg, 0.171 mmol) in THF (30 mL). The reaction mixture was stirred at 60 °C for 1.5 h under a nitrogen atmosphere. After completion of the reaction, the mixture was poured into an aqueous HCl solution (2 M, 20 mL) to quench the reaction. The resulting precipitate was collected by filtration and washed with water. A red solid was obtained (51.0 mg, 49.9%).

^{1}H NMR (500 MHz, $CDCl_3$) δ 8.70 (dd, J = 8.0, 2.3 Hz, 2H), 8.58–8.53 (m, 4H), 8.29–8.27 (m, 2H), 7.96 (d, J = 8.6 Hz, 1H), 7.69–7.63 (m, 4H), 7.49 (t, J = 7.7 Hz, 1H), 7.35 (d, J = 8.0 Hz, 2H), 2.80–2.75 (m, 2H), 1.18 (d, J = 6.9 Hz, 12H).

Synthesis of CdS NCs.[5]

CdO (520 mg, 4.05 mmol), oleic acid (12 mL), and 1-octadecene (18 mL) were loaded into a three-necked flask. The mixture was degassed under vacuum at 90 °C for 1 h. After degassing, the reaction mixture was heated to 220 °C under a nitrogen atmosphere with stirring until the solution became clear and colorless, indicating the formation of a cadmium oleate complex. Separately, sulfur powder (70.0 mg, 2.18 mmol) was dissolved in 1-octadecene (8 mL) at 50 °C to prepare a sulfur precursor solution. This sulfur solution was injected into the cadmium oleate solution at 220 °C. Immediately after injection, the reaction mixture was stirred at 220 °C for 3 min, after which the temperature was gradually lowered to 180 °C over 4 min. The reaction mixture was further stirred at 180 °C for 3 min and then cooled to room temperature under

continuous stirring, yielding a pale-yellow solution. The solution was extracted using a mixed solvent of methanol and hexane (v/v = 1:0.7). The hexane phase was collected and further extracted with methanol and hexane (v/v = 1:2). The organic fraction was precipitated by the addition of excess acetone. The precipitated CdS NCs were collected and redispersed in $CHCl_3$.

Synthesis of ZnS NCs.[6]

Zinc stearate (1.26 g, 2.02 mmol), oleylamine (17.0 mL, 52.8 mmol), and 1-octadecene (23.0 mL) were loaded into a 300 mL three-necked flask (Zn precursor). The mixture was degassed under vacuum at 90 °C for 1 h and then heated to 170 °C under a nitrogen atmosphere with stirring for 1 h. In a separate 50 mL two-neck flask, sulfur powder (65.0 mg, 2.03 mmol) and 1-octadecene (8.0 mL) were loaded (S precursor). The mixture was degassed under vacuum at 65 °C for 1 h and subsequently filled with nitrogen. The sulfur precursor maintained at 65 °C was swiftly injected into the Zn precursor heated at 230 °C. The reaction mixture was stirred at 230 °C for 5 min and then allowed to cool to room temperature. Upon cooling, a pale-yellow suspension formed with a white precipitate. The crude mixture was centrifuged (9,000 rpm, 10 min) twice to separate the white precipitate from the yellow supernatant. The supernatant was further centrifuged (9,000 rpm, 10 min) to remove residual solids. The NCs were precipitated from the clarified supernatant by adding excess acetone and collected by centrifugation (9,000 rpm, 5 min). The precipitate was redispersed in a small amount of $CHCl_3$, followed by addition of excess methanol to reprecipitate the NCs. After centrifugation (9,000 rpm, 5 min) and decantation twice, the final product was dried under vacuum at room temperature.

3. ^{1}H NMR spectra

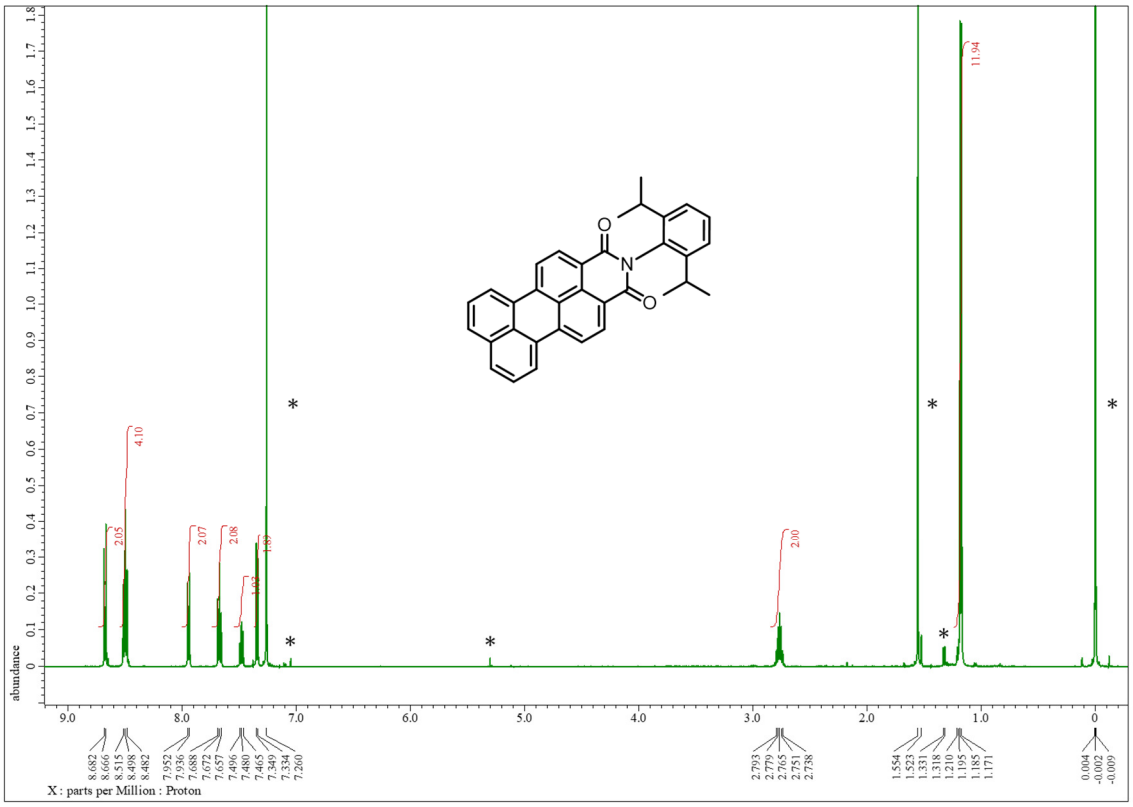

Figure S1. ^{1}H NMR (500 MHz) spectrum of compound **1** in $CDCl_3$ (* solvent peaks).

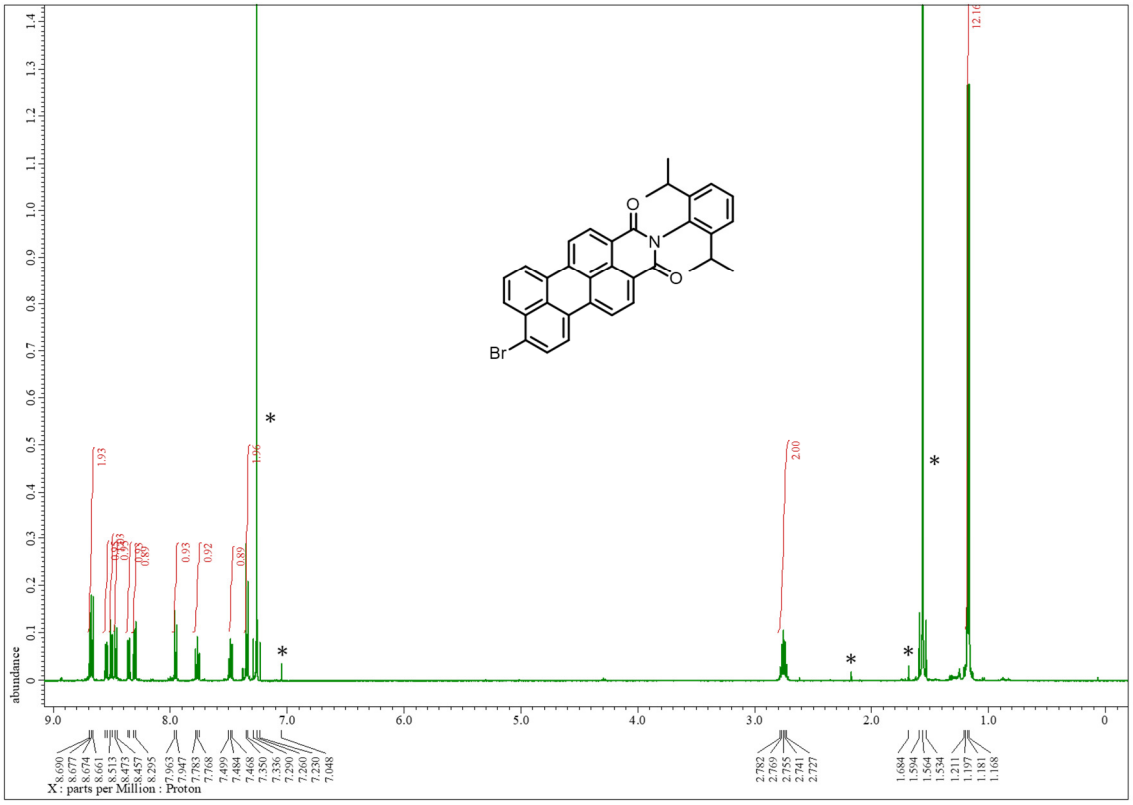

Figure S2. ^{1}H NMR (500 MHz) spectrum of compound **2** in $CDCl_3$ (* solvent peaks).

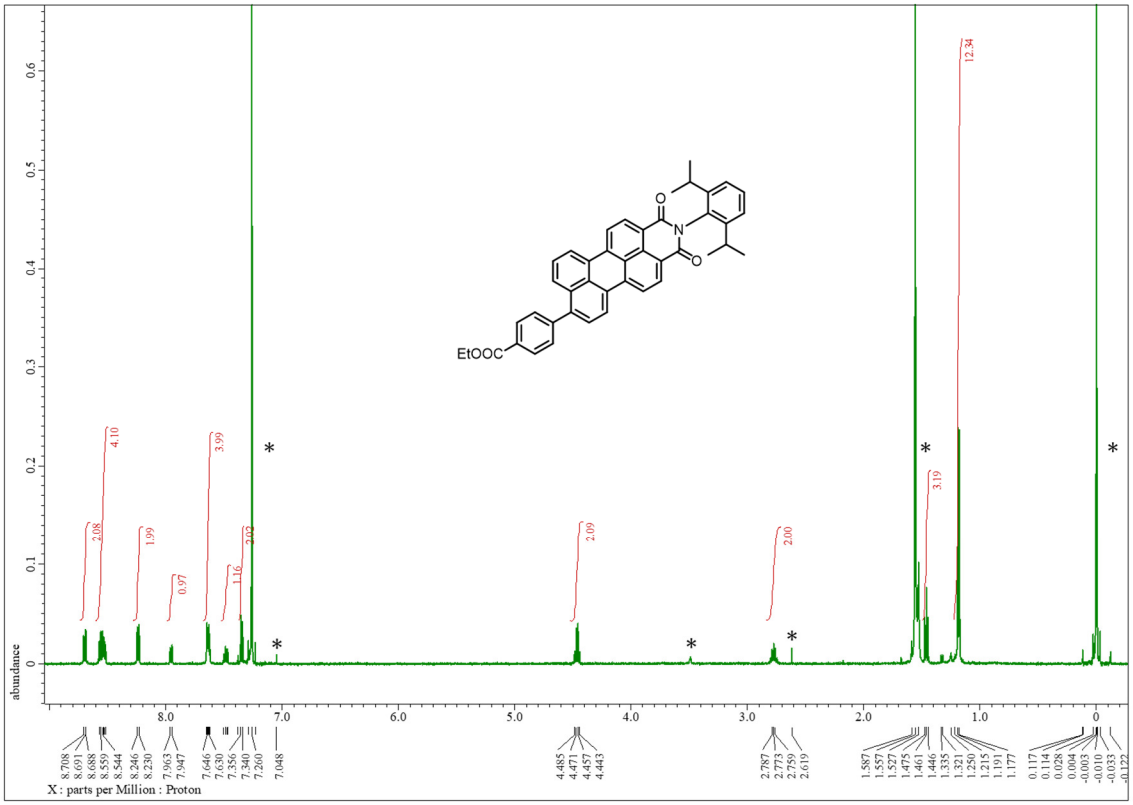

Figure S3. ^{1}H NMR (500 MHz) spectrum of compound **3** in $CDCl_3$ (* solvent peaks).

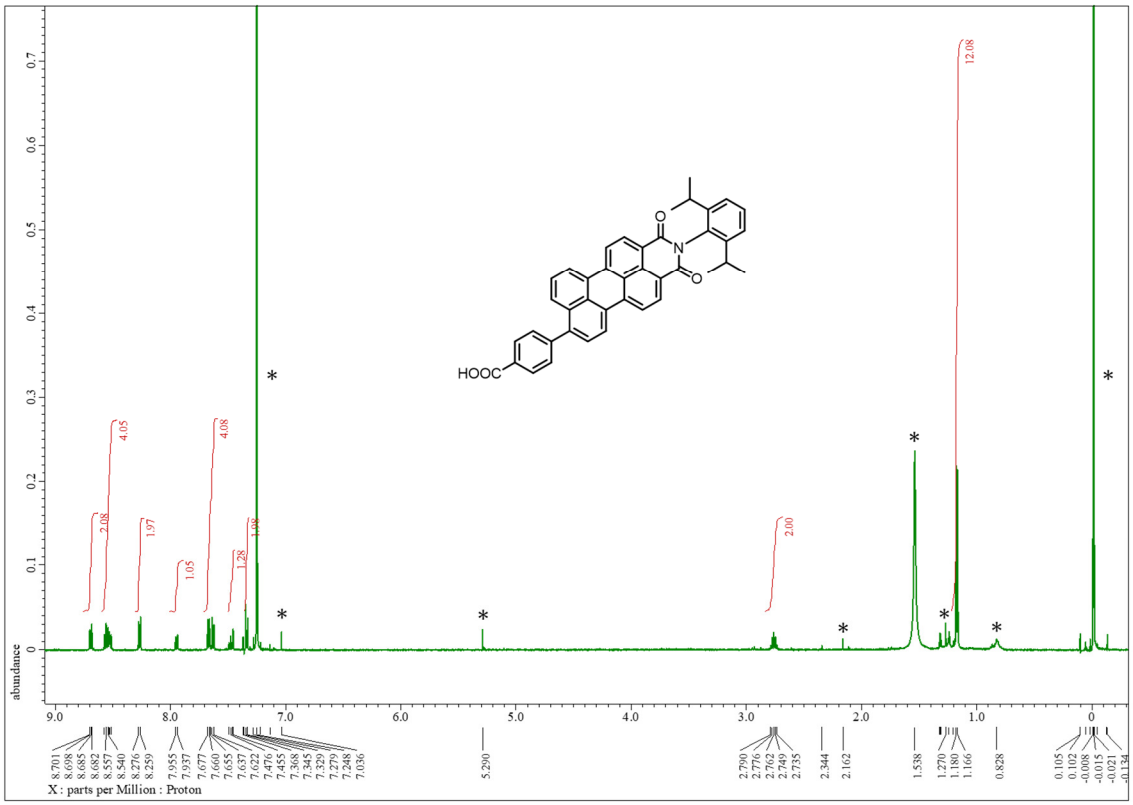

Figure S4. ^{1}H NMR (500 MHz) spectrum of PMI in $CDCl_3$ (* solvent peaks).

4. HPLC chromatograms

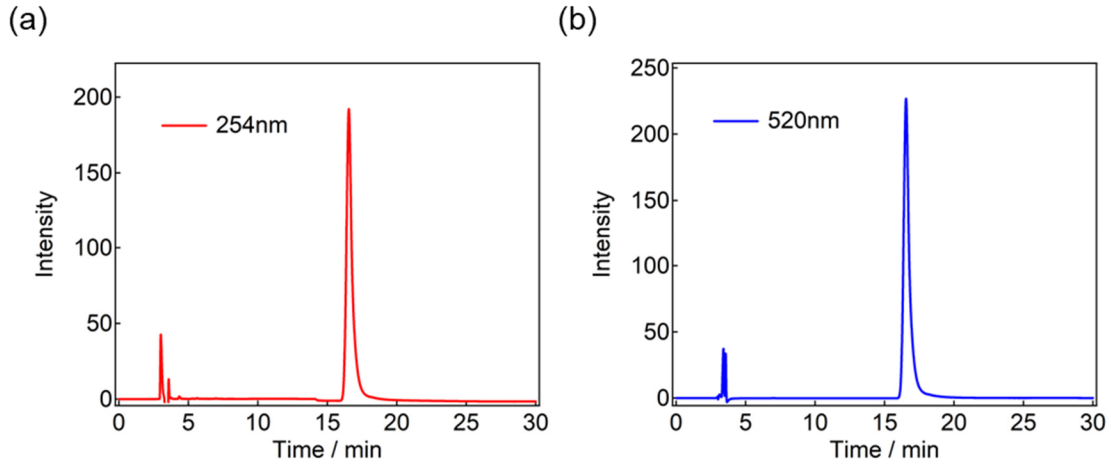

Figure S5. HPLC chromatograms of PMI monitored at (a) 254 nm and (b) 520 nm, both indicating 99% purity. The analysis was performed using an analytical column (Mightysil RP-18GP II, 25 cm × 4.6 mm, 5 µm particle; Kanto Chemical Co., Inc.) equipped with a photodiode array (PDA) detector. The mobile phase was ethyl acetate/hexane (v/v = 2:5) at a flow rate of 1.0 mL/min. Peaks observed below 5 min originate from the injection solvent.

5. Powder XRD patterns

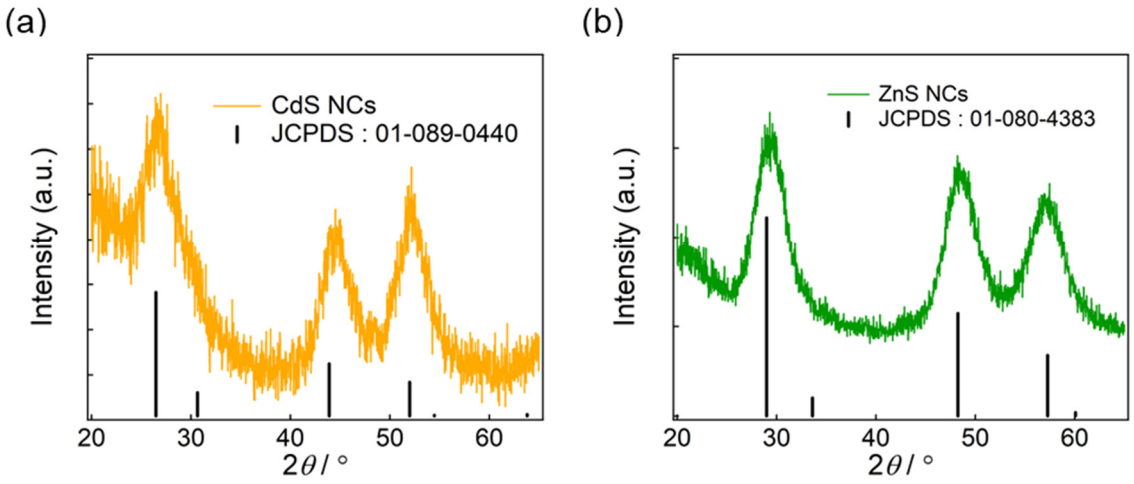

Figure S6. Powder XRD patterns of (a) CdS NCs and (b) ZnS NCs.

6. Steady-state absorption spectra

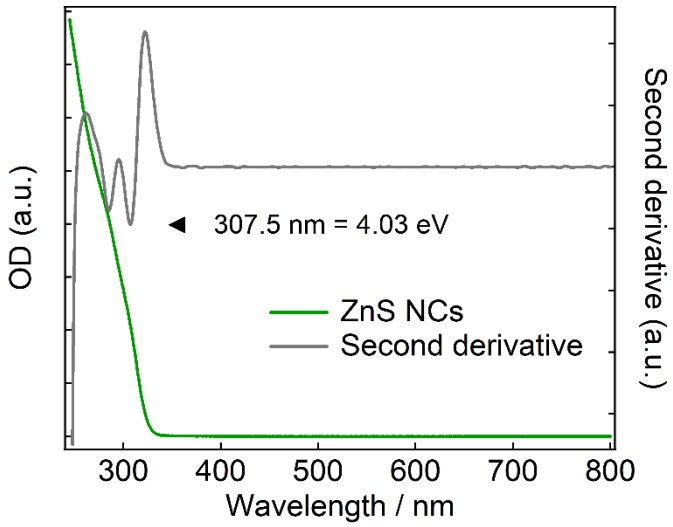

Figure S7. Steady-state absorption spectra of ZnS NCs in $CHCl_3$. The first excitonic absorption peaks were determined from second-derivative analysis of the corresponding absorption spectra.

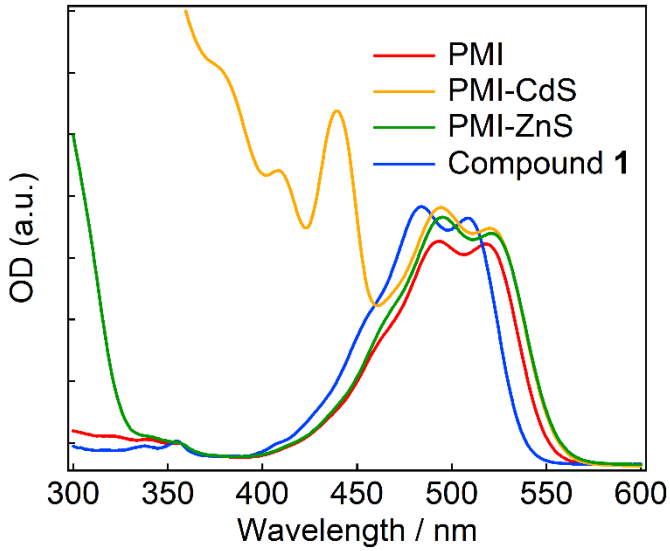

Figure S8. Steady-state absorption spectra of PMI, PMI-CdS, PMI-ZnS, and compound 1 in $CHCl_3$.

7. TEM images

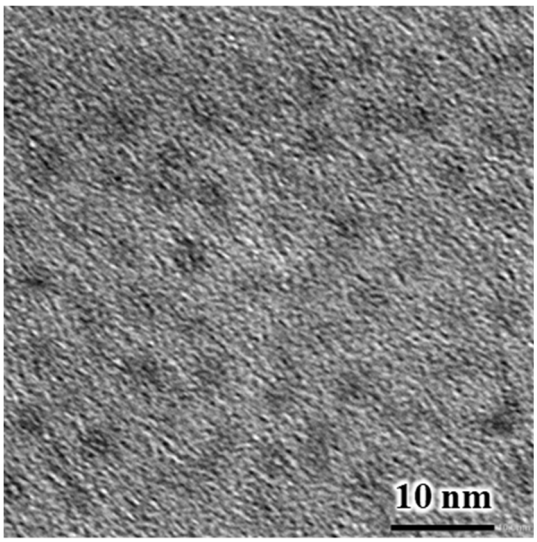

Figure S9. TEM images of ZnS NCs.

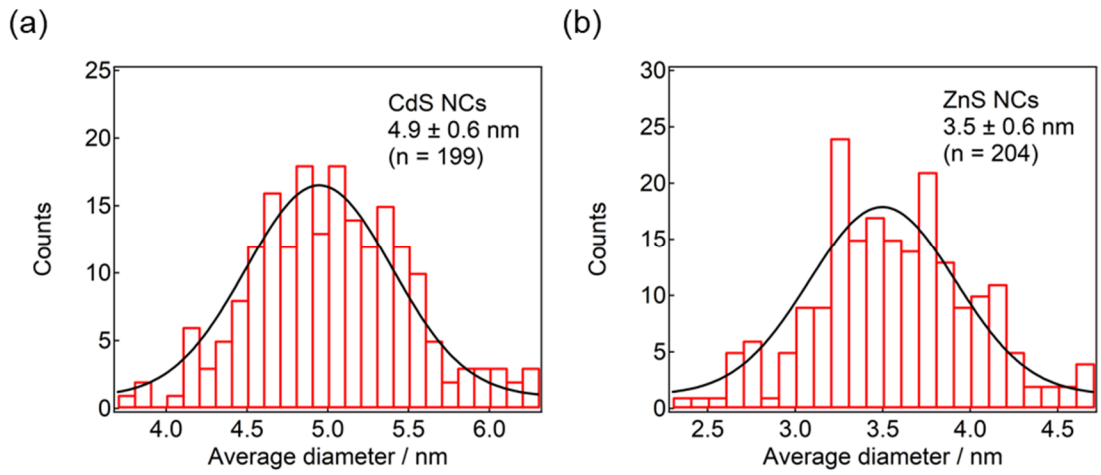

Figure S10. The average diameters of (a) CdS NCs and (b) ZnS NCs determined from TEM images.

8. Molar absorption coefficients of PMI

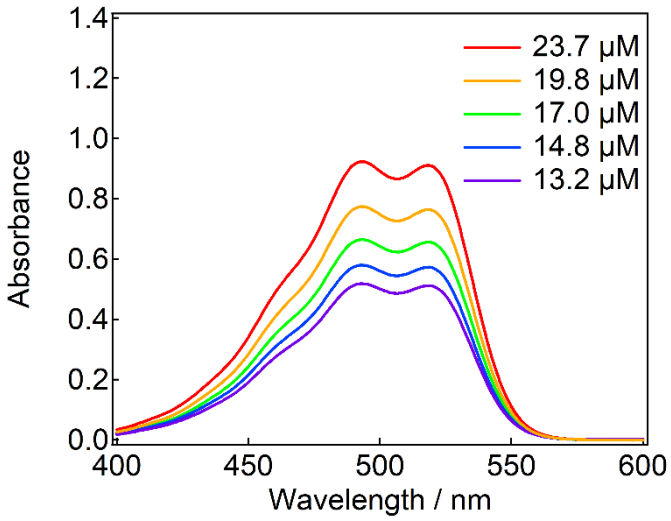

Figure S11. Absorption spectra of PMI in $CHCl_3$ at various concentrations.

Table S1. Molar absorption coefficients of PMI in $CHCl_3$.

wavelength (nm)	ε ($\times 10^4$ M^{-1} L^{-1})	wavelength (nm)	ε ($\times 10^4$ M^{-1} L^{-1})
490	3.87	510	3.71
491	3.89	511	3.73
492	3.91	512	3.75
493	3.91	513	3.78
494	3.91	514	3.80
495	3.90	515	3.82
496	3.88	516	3.84
497	3.86	517	3.86
498	3.84	518	3.86
499	3.81	519	3.86
500	3.78	520	3.85
501	3.75	521	3.82
502	3.73	522	3.79
503	3.71	523	3.74
504	3.69	524	3.68
505	3.68	525	3.60
506	3.67	526	3.51
507	3.67	527	3.41
508	3.68	528	3.29
509	3.69	529	3.17

9. Cyclic voltammetry of PMI

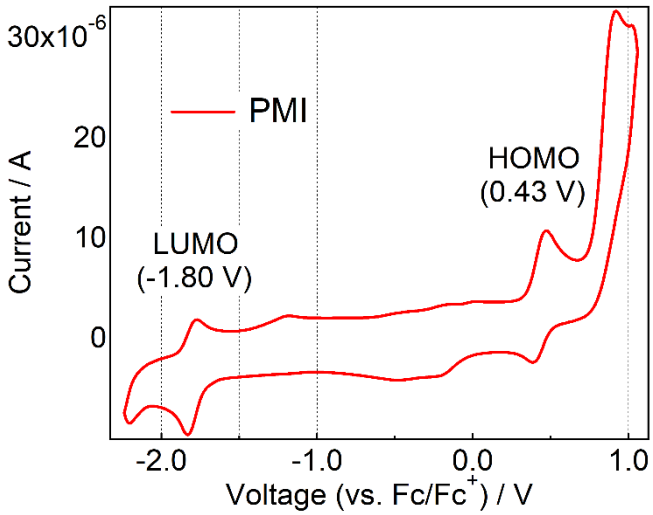

Figure S12. Cyclic voltammograms of PMI in acetonitrile containing 0.1 M $TBAPF_6$ as the supporting electrolyte. The PMI concentration was 1.0 mM, and the potential scan rate was 0.1 V/s.

The LUMO levels and higher excited-state energy levels of PMI and PBI shown in Figure 1 are schematic estimates. The LUMO level of PMI was calculated from the reduction potential obtained from cyclic voltammograms (Figure S12). In contrast, the LUMO level of PBI was estimated from the reduction potentials reported in previous studies for structurally related PBI derivatives.[7] Higher excited-state energy levels were estimated by adding the photon energy of the push pulse used in the experiment to the S_1 energy. For example, the 650-nm push pulse used for PMI corresponds to ~1.9 eV.

10. Steady-state fluorescence spectroscopy

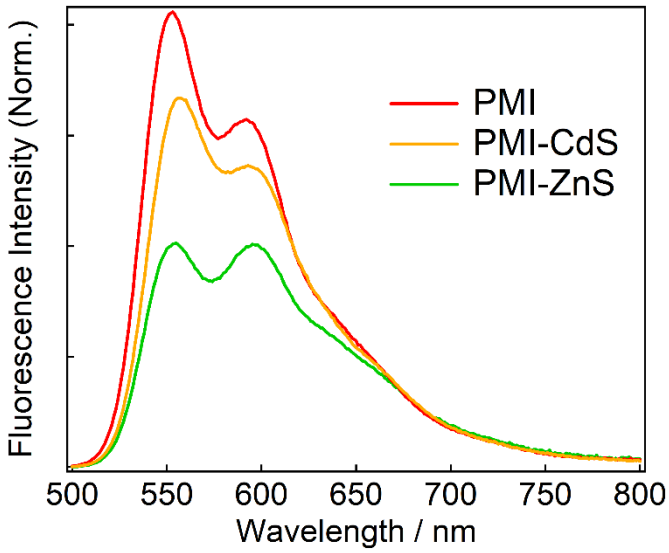

Figure S13. Steady-state fluorescence spectra of PMI, PMI-CdS, and PMI-ZnS excited at 488 nm in CHCl3. The spectra were normalized by the absorbance at the excitation wavelength.

Table S2. Fluorescence quantum yield (***Φ*F**) of PMI, PMI-CdS, and PMI-ZnS.

Sample	***Φ*F**
PMI	1.0
PMI-CdS	0.88
PMI-ZnS	0.62

11. ^{1}H NMR measurements of PMI-NCs

To examine whether PMI binds to the surfaces of the NCs in solution, ^{1}H NMR spectra of PMI, PMI-CdS, CdS NCs, PMI-ZnS, and ZnS NCs were recorded. $CDCl_3$ was used as the solvent, and the samples were prepared as illustrated in Figure S14. Upon addition of the NCs, the signals derived from PMI exhibited chemical-shift changes and pronounced line broadening. Such shifts in the signals of organic ligands bound to NCs are generally attributed not only to changes in electron density upon coordination to surface metal ions but also to differences in the solvation environment between free and bound ligands.[8] In addition, line broadening of the bound ligands is known to arise from reduced rotational mobility upon binding to the nanocrystal surface, which accelerates T_2 relaxation. Therefore, these spectral changes indicate that PMI binds to the NC surfaces in solution.

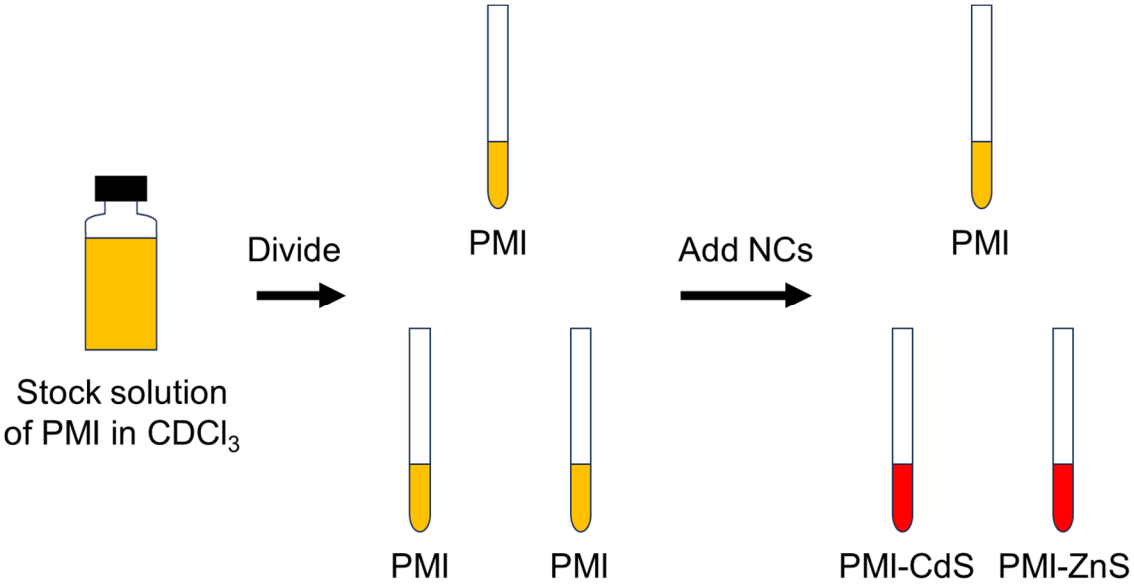

Figure S14. Preparation of PMI and PMI-NCs in $CDCl_3$ for ^{1}H NMR measurements.

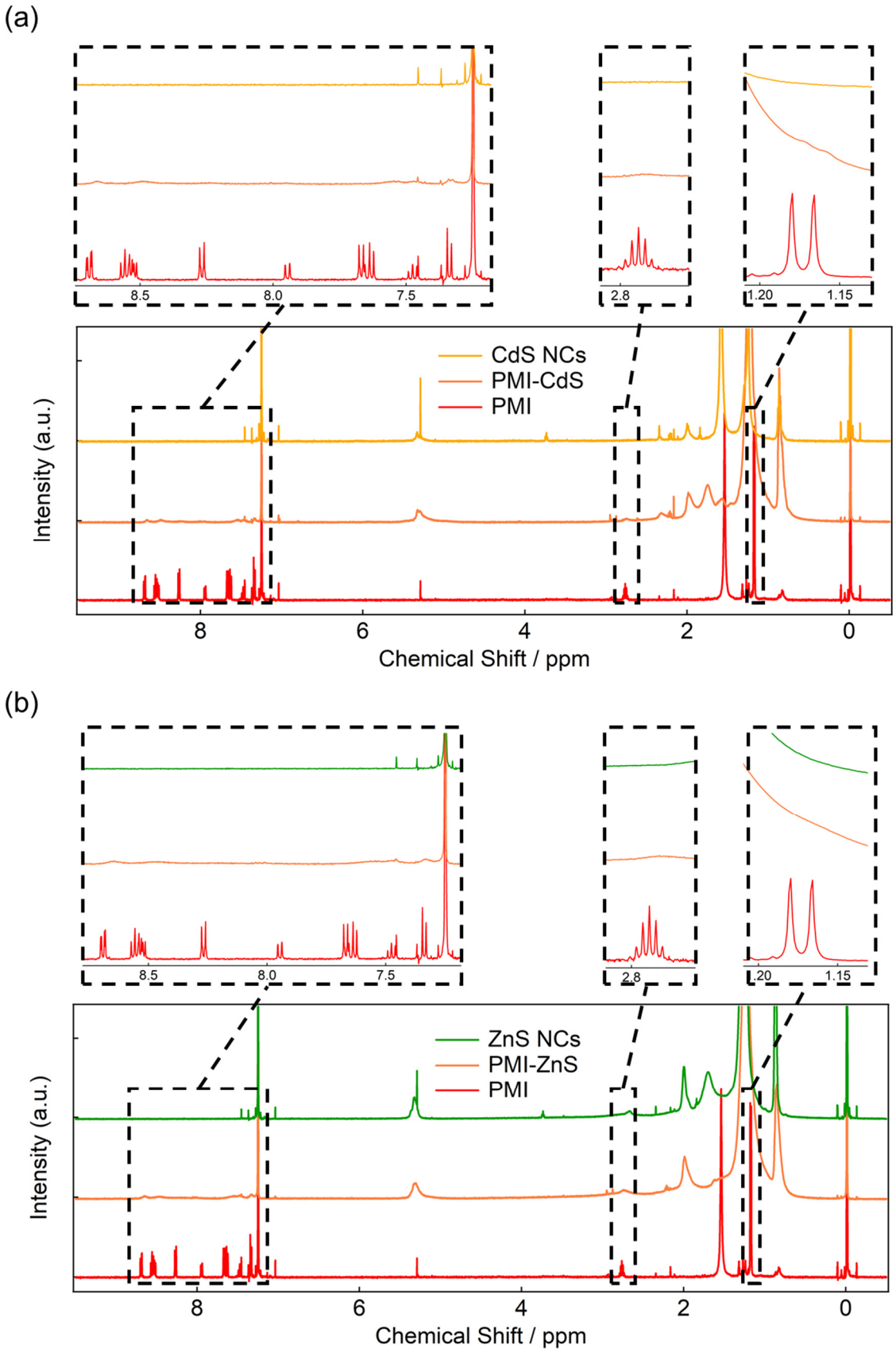

Figure S15. ^{1}H NMR spectra of (a) PMI and PMI-CdS and (b) PMI and PMI-ZnS in $CDCl_3$. The ^{1}H NMR spectra of bare CdS and ZnS NCs are overlaid for comparison.

12. DOSY measurements

To evaluate the effect of the carboxylic acid moiety of PMI on its association behavior in solution, DOSY measurements were performed in $CDCl_3$ at 18.6 °C. Diffusion coefficients (D) were determined from each NMR signal of PMI and compound **1**, and the averaged values were calculated to be $D_{PMI} = 6.23\times10^{-10}$ m^2 s^{-1} and $D_1 = 7.31\times10^{-10}$ m^2 s^{-1}, respectively. The theoretical diffusion coefficients were estimated from the Stokes–Einstein equation shown below, giving $D_{PMI} = 6.90\times10^{-10}$ m^2 s^{-1} and $D_1 = 7.24\times10^{-10}$ m^2 s^{-1}, where the molecular volume (V_{PMI} = 394.482 cm^3 mol^{-1}, V_1 = 338.924 cm^3 mol^{-1}) was obtained from DFT calculations (B3LYP/6-31+G(d,p)). The diffusion coefficients of PMI were broadly distributed over the range of 3.8–7.5×10^{-10} m^2 s^{-1}, whereas those of compound **1** were confined to a narrower range of 7.2–8.4×10^{-10} m^2 s^{-1}. Because carboxylic acid groups are known to form intermolecular associations in solution, the broad distribution observed for PMI likely reflects an equilibrium between monomeric and associated species. In contrast, compound **1**, which lacks a carboxylic acid moiety, does not exhibit such broadening and is considered to exist predominantly as a monomer in solution.

$$D = \frac{k_B T}{6\pi\eta R} \quad (\mathrm{m^2\ s^{-1}})$$

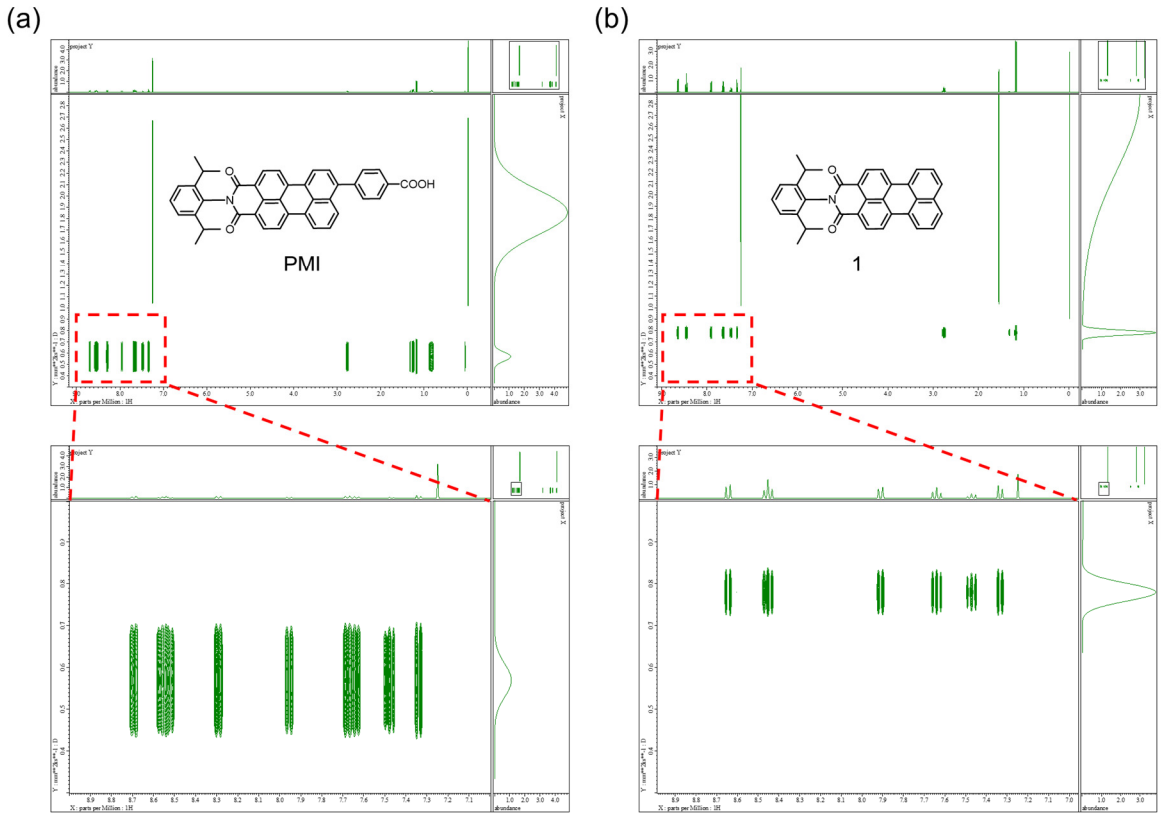

Figure S16. DOSY spectra of (a) PMI and (b) compound **1** in $CDCl_3$.

13. Femtosecond to picosecond transient absorption measurements

The first pump pulse was centered at 520 nm with a beam-spot diameter of 184 μm, and the second push pulse was centered at 650 nm with a beam-spot diameter of 233 μm.

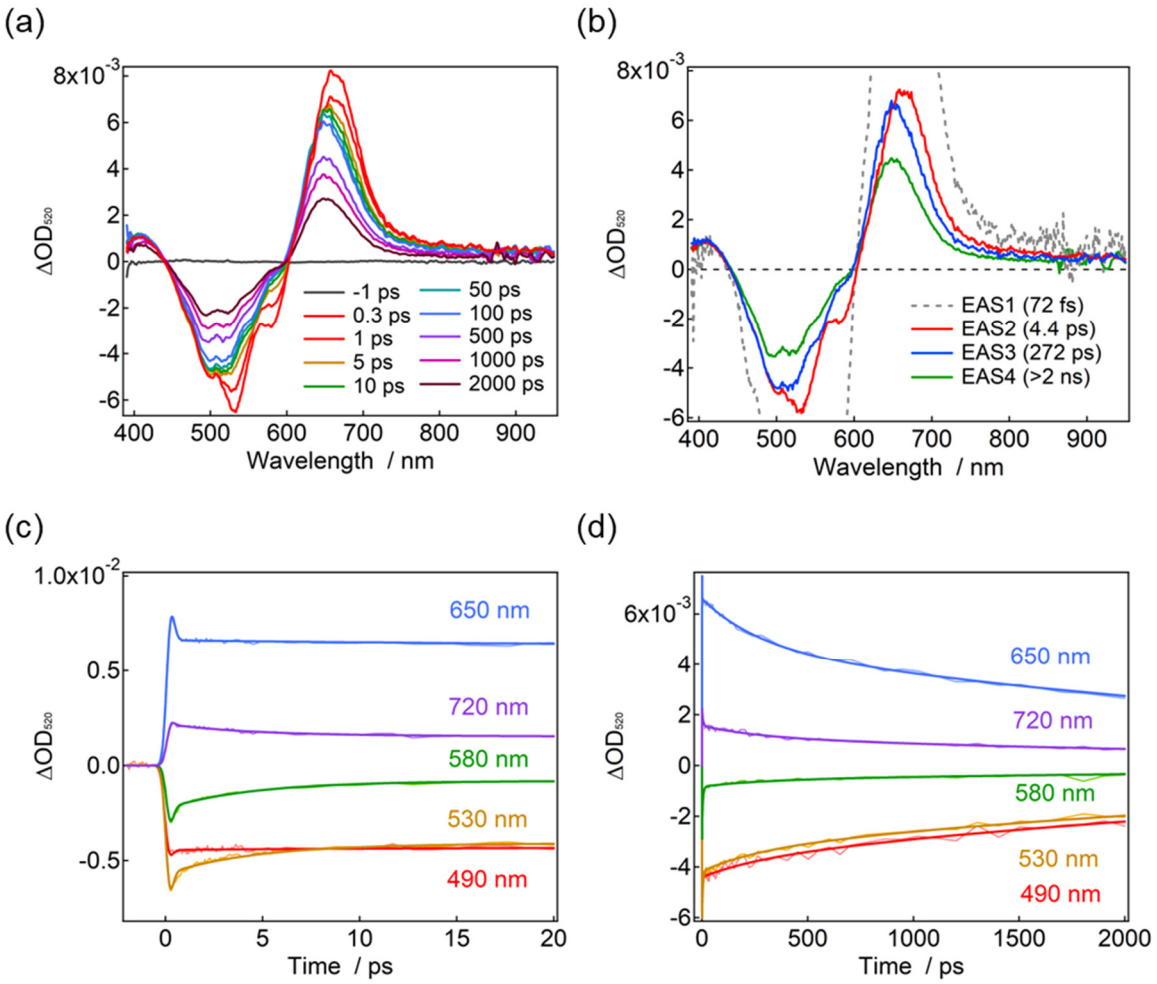

Figure S17. (a) Femtosecond to nanosecond transient absorption spectra and (b) evolution-associated spectra (EAS) of PMI in $CHCl_3$ excited with 520-nm femtosecond laser pulse (30 nJ $pulse^{-1}$). Times shown in brackets indicate the time constant of each EAS species. (c) Short-time and (d) long-time dynamics. The thick red, yellow, green, blue, and purple lines represent the fitting curves obtained from SVD-based global analysis using a four-state sequential kinetic model.

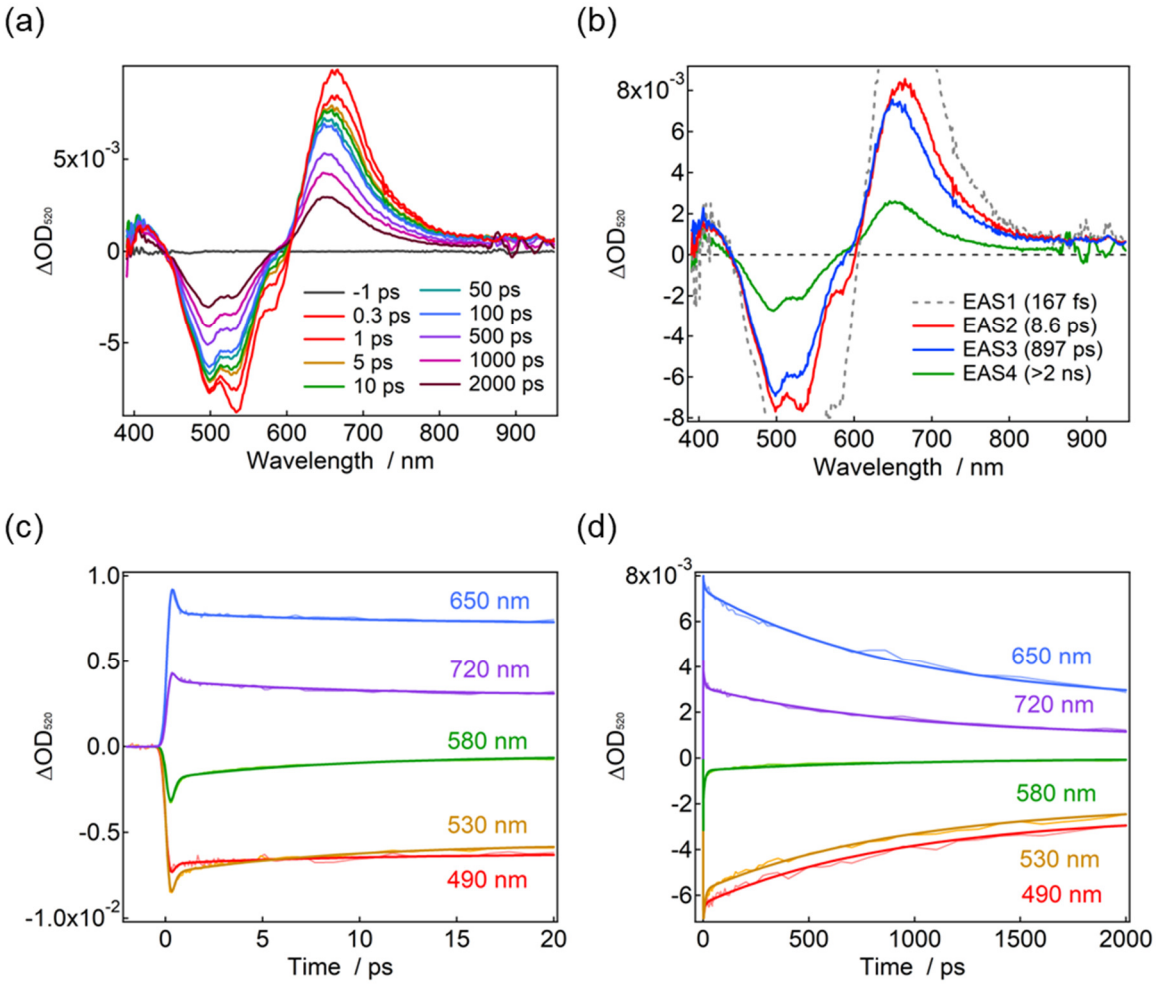

Figure S18. (a) Femtosecond to nanosecond transient absorption spectra and (b) evolution-associated spectra (EAS) of PMI-CdS in $CHCl_3$ excited with a 520-nm femtosecond laser pulse (30 nJ $pulse^{-1}$). Times shown in brackets indicate the time constant of each EAS species. (c) Short-time and (d) long-time dynamics. The thick red, yellow, green, blue, and purple lines represent the fitting curves obtained from SVD-based global analysis using a four-state sequential kinetic model.

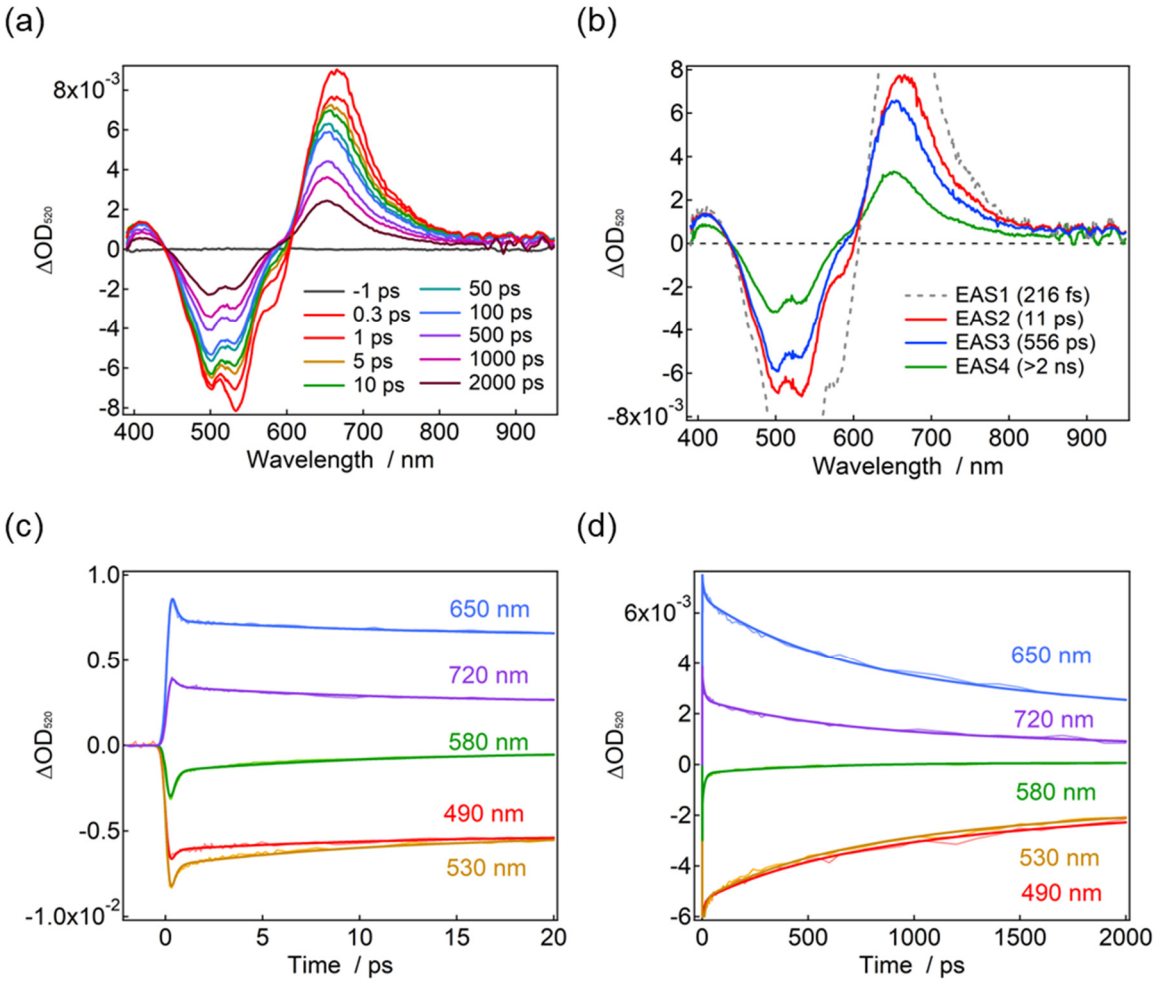

Figure S19. (a) Femtosecond to nanosecond transient absorption spectra and (b) evolution-associated spectra (EAS) of PMI-ZnS in $CHCl_3$ excited with a 520-nm femtosecond laser pulse (30 nJ $pulse^{-1}$). Times shown in brackets indicate the time constant of each EAS species. (c) Short-time and (d) long-time dynamics. The thick red, yellow, green, blue, and purple lines represent the fitting curves obtained from SVD-based global analysis using a four-state sequential kinetic model.

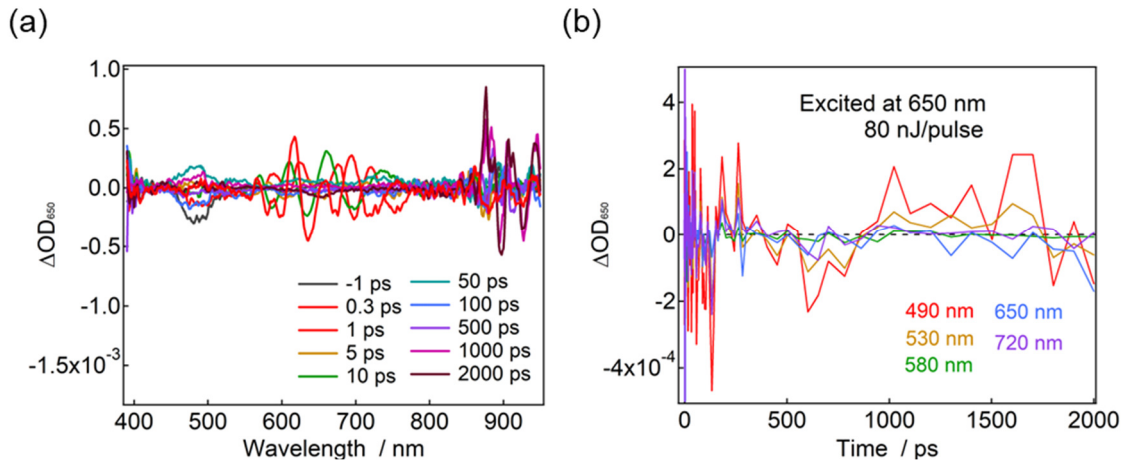

Figure S20. Femtosecond to nanosecond transient absorption (a) spectra and (b) dynamics of PMI in $CHCl_3$ excited with 650-nm femtosecond laser pulse (80 nJ $pulse^{-1}$).

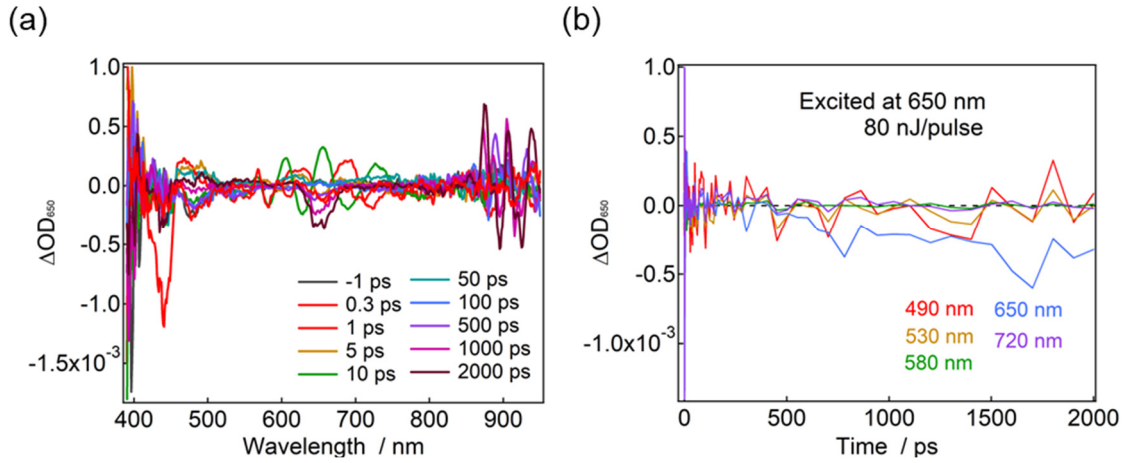

Figure S21. Femtosecond to nanosecond transient absorption (a) spectra and (b) dynamics of PMI-CdS in $CHCl_3$ excited with 650-nm femtosecond laser pulse (80 nJ $pulse^{-1}$).

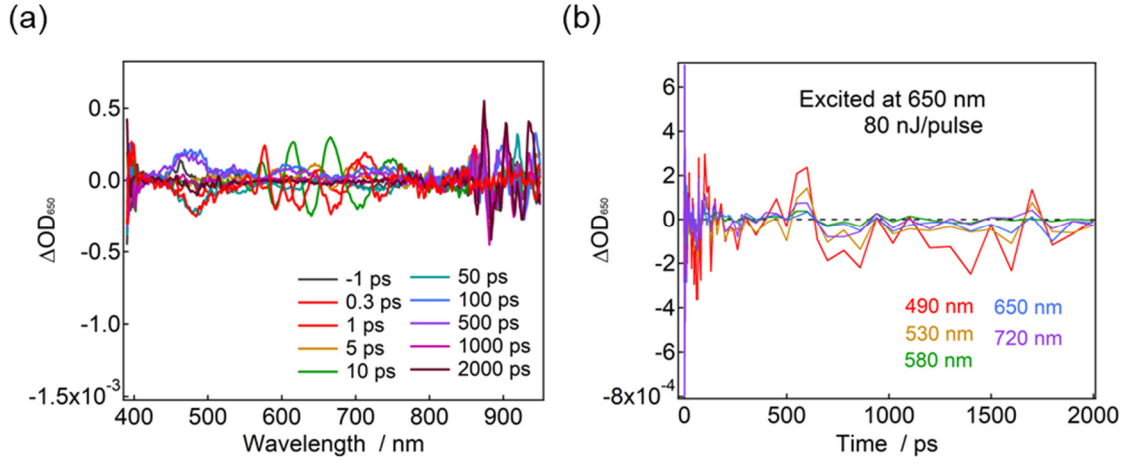

Figure S22. Femtosecond to nanosecond transient absorption (a) spectra and (b) dynamics of PMI-ZnS in $CHCl_3$ excited with 650-nm femtosecond laser pulse (80 nJ $pulse^{-1}$).

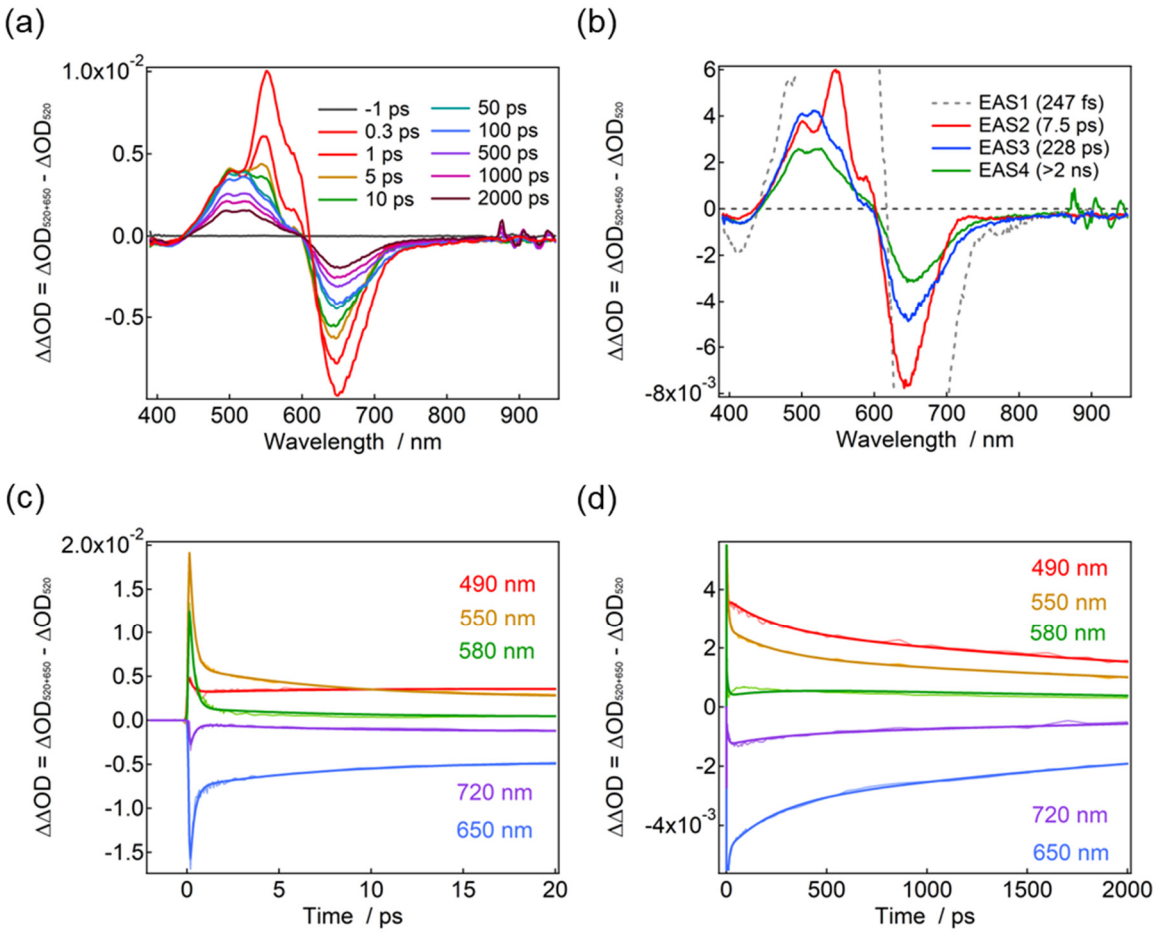

Figure S23. (a) Femtosecond to nanosecond transient absorption spectra and (b) evolution-associated spectra (EAS) of PMI in $CHCl_3$ excited with the first pulse set to 520 nm (250 nJ pulse^{-1}), while the second pulse was set to 650 nm (80 nJ pulse^{-1}), and the time delay between the excitation pulses was fixed to 5 ps. Times shown in brackets indicate the time constant of each EAS species. (c) Short-time and (d) long-time dynamics. The thick red, yellow, green, blue, and purple lines represent the fitting curves obtained from SVD-based global analysis using a four-state sequential kinetic model.

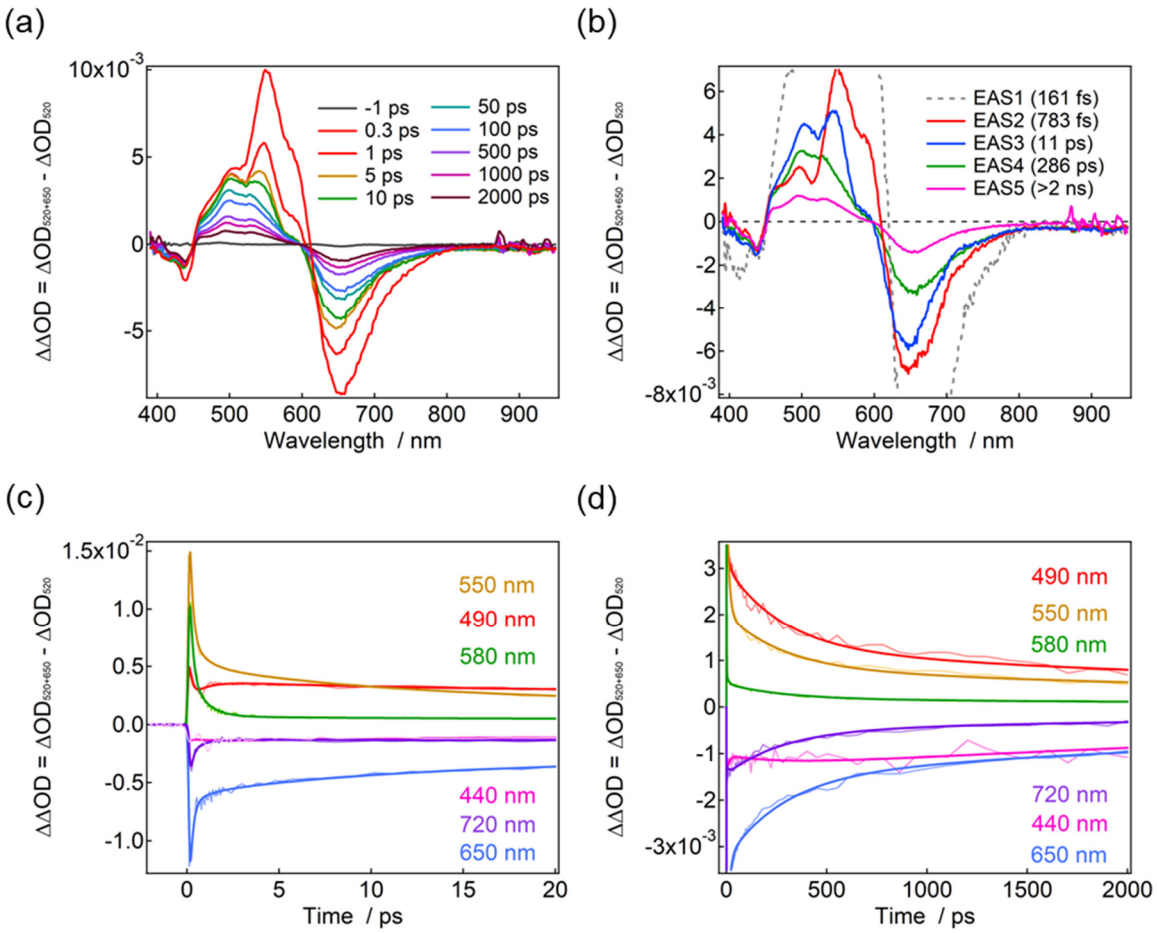

Figure S24. (a) Femtosecond to nanosecond transient absorption spectra and (b) evolution-associated spectra (EAS) of PMI-CdS in $CHCl_3$, excited with the first pulse set to 520 nm (250 nJ pulse^{-1}), while the second pulse was set to 650 nm (80 nJ pulse^{-1}) and the time delay between the excitation pulses was fixed to 5 ps. Times shown in brackets indicate the time constant of each EAS species. (c) Short-time and (d) long-time dynamics. The thick red, yellow, green, blue, pink, and purple lines represent the fitting curves obtained from SVD-based global analysis using a five-state sequential kinetic model.

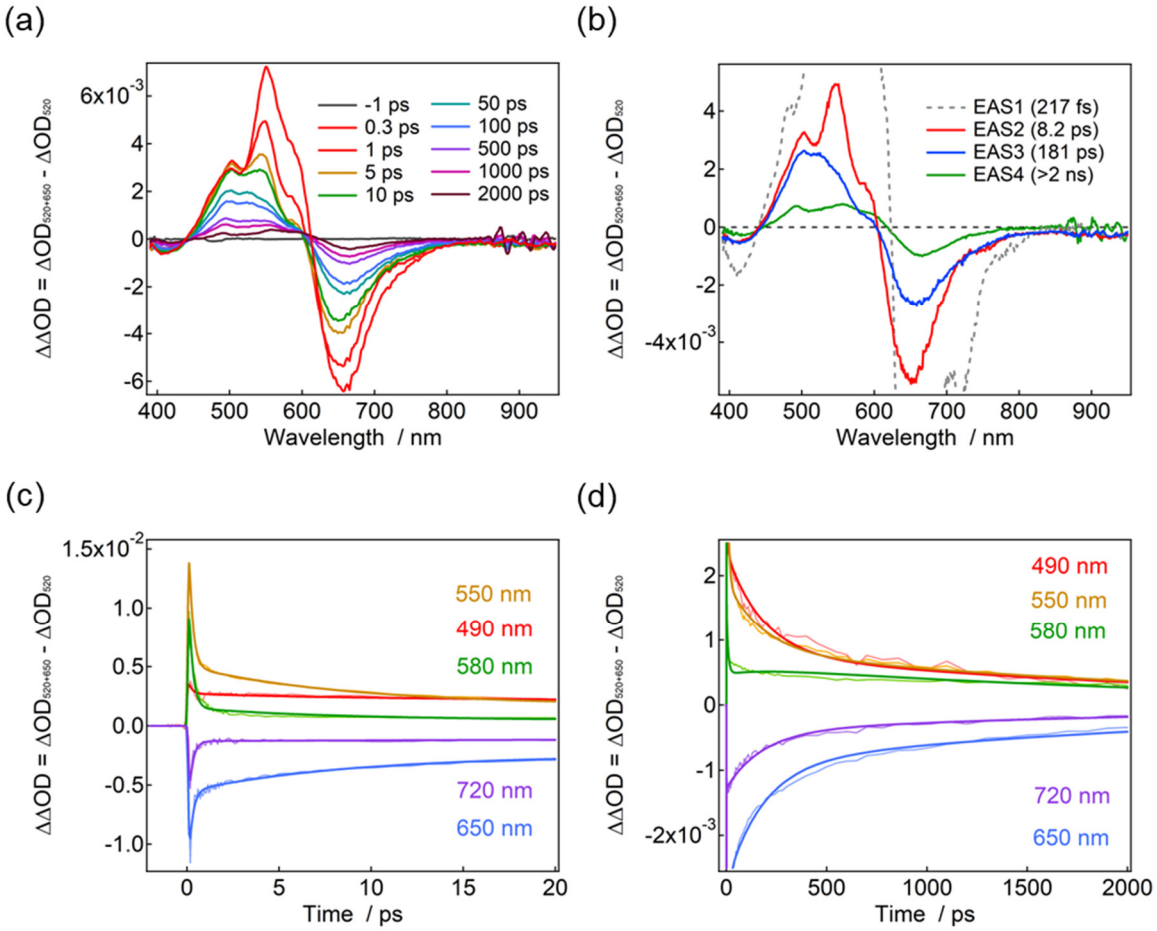

Figure S25. (a) Femtosecond to nanosecond transient absorption spectra and (b) evolution-associated spectra (EAS) of PMI-ZnS in $CHCl_3$, excited with the first pulse set to 520 nm (250 nJ $pulse^{-1}$), while the second pulse was set to 650 nm (80 nJ $pulse^{-1}$) and the time delay between the excitation pulses was fixed to 5 ps. Times shown in brackets indicate the time constant of each EAS species. (c) Short-time and (d) long-time dynamics. The thick red, yellow, green, blue, and purple lines represent the fitting curves obtained from SVD-based global analysis using a four-state sequential kinetic model.

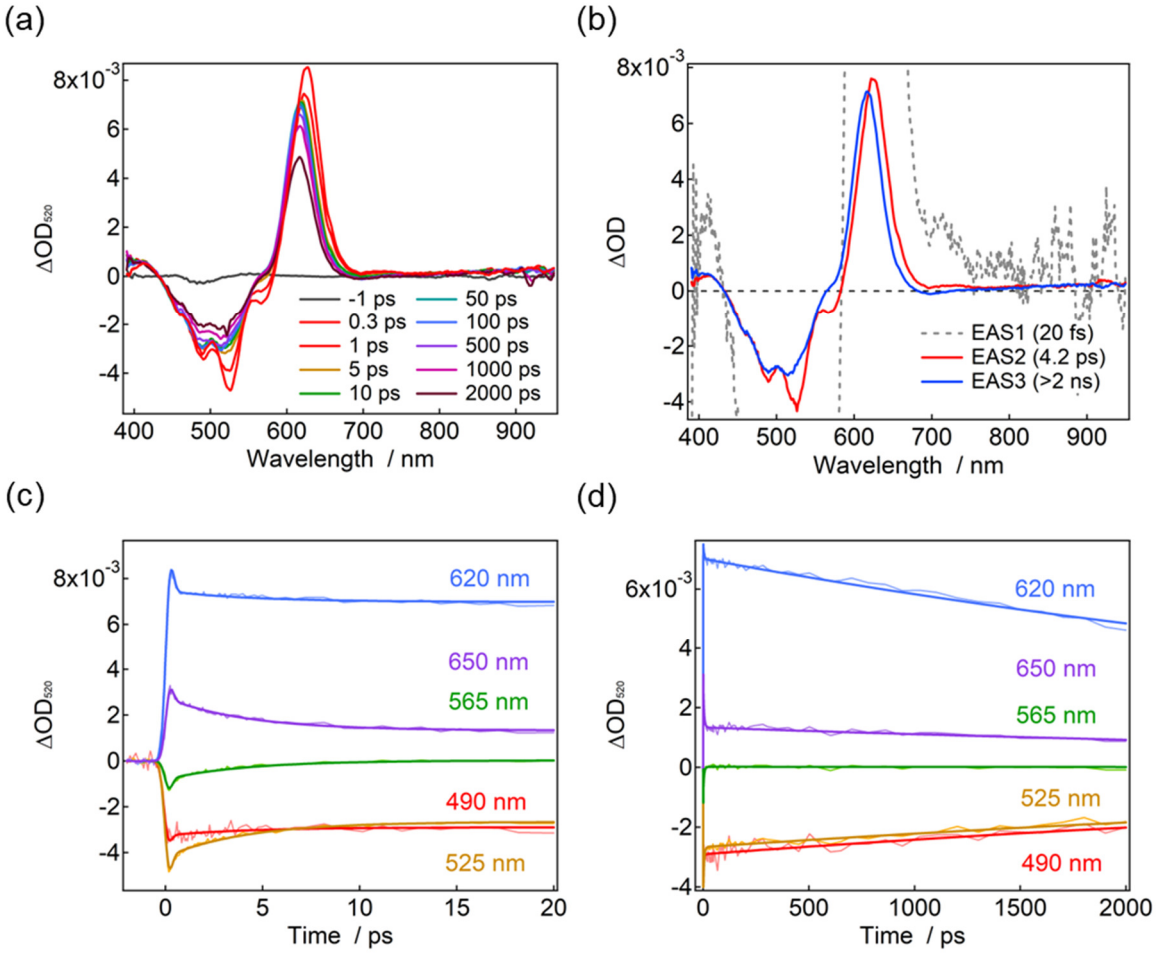

Figure S26. (a) Femtosecond to nanosecond transient absorption spectra and (b) evolution-associated spectra (EAS) of compound **1** in $CHCl_3$ excited with a 520-nm femtosecond laser pulse (40 nJ pulse^{-1}). Times shown in brackets indicate the time constant of each EAS species. (c) Short-time and (d) long-time dynamics. The thick red, yellow, green, blue, and purple lines represent the fitting curves obtained from SVD-based global analysis using a four-state sequential kinetic model.

Upon excitation of PMI-CdS with a 347 nm pump pulse, CdS NCs can be excited almost selectively (Figure S27). Immediately after photoexcitation, a sharp and intense negative signal was observed at 440 nm, together with a positive signal at 460 nm. These signals are assigned to the ground-state bleach of the first excitonic absorption band of CdS NCs and the formation of the excited state, respectively. These spectral features are consistent with those reported in previous studies. The negative signals were observed at 496 and 524 nm, together with a positive signal at 650 nm from 300 fs to 40 ps, and the overall spectral profile was similar to the transient absorption spectrum of PMI. Considering the electrochemical results of PMI and the energy-level diagram based on previous studies on CdS NCs, these observations strongly suggest that the electrons and holes generated immediately after photoexcitation of CdS NCs are transferred to PMI.[9]

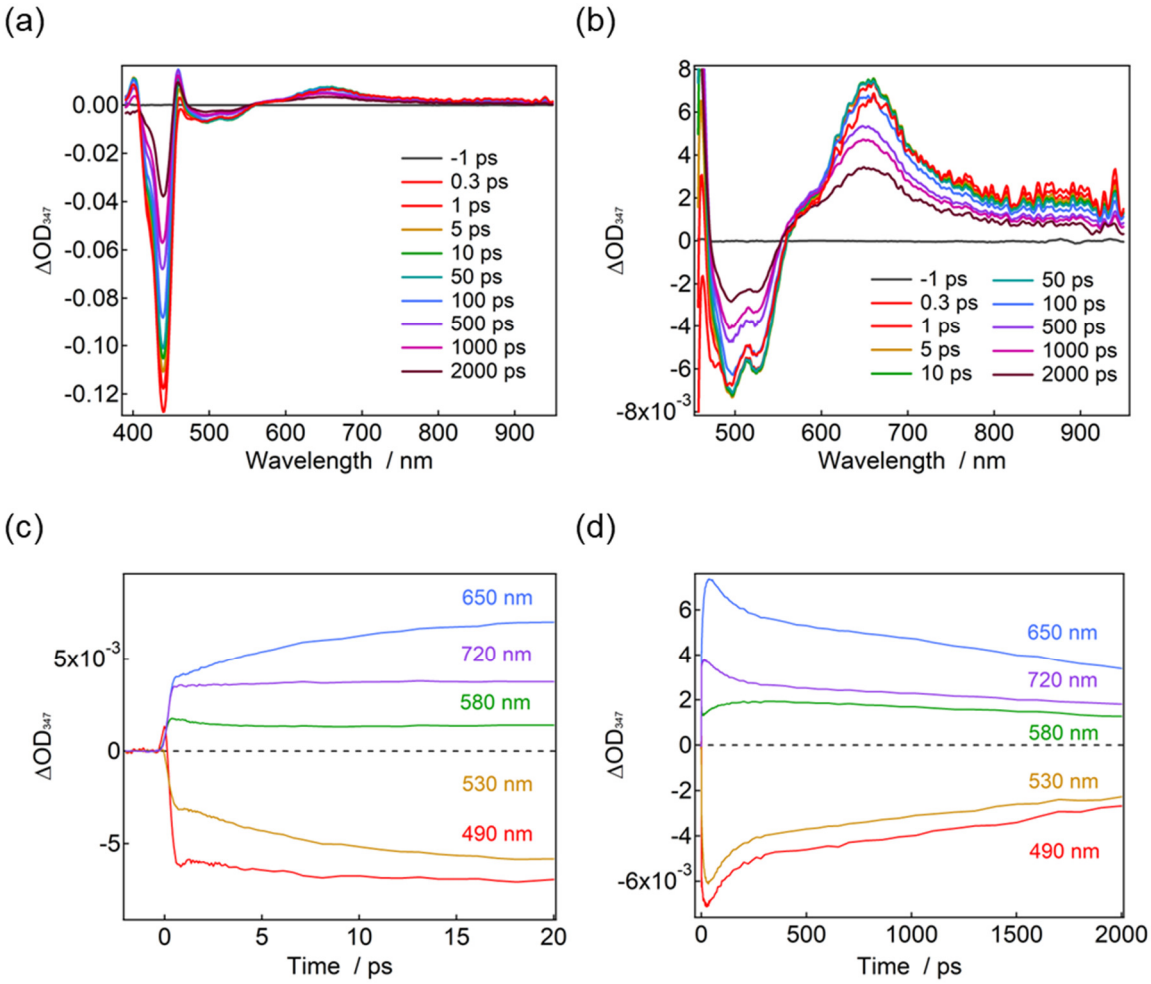

Figure S27. Femtosecond-to-nanosecond transient absorption spectra of PMI-CdS in $CHCl_3$ excited with 347-nm femtosecond laser pulse (60 nJ $pulse^{-1}$); (a) 390–950 nm, (b) 450–950 nm. (c) The short-time and (d) long-time dynamics.

Excitation intensity dependence of the double-pulse transient absorption spectra

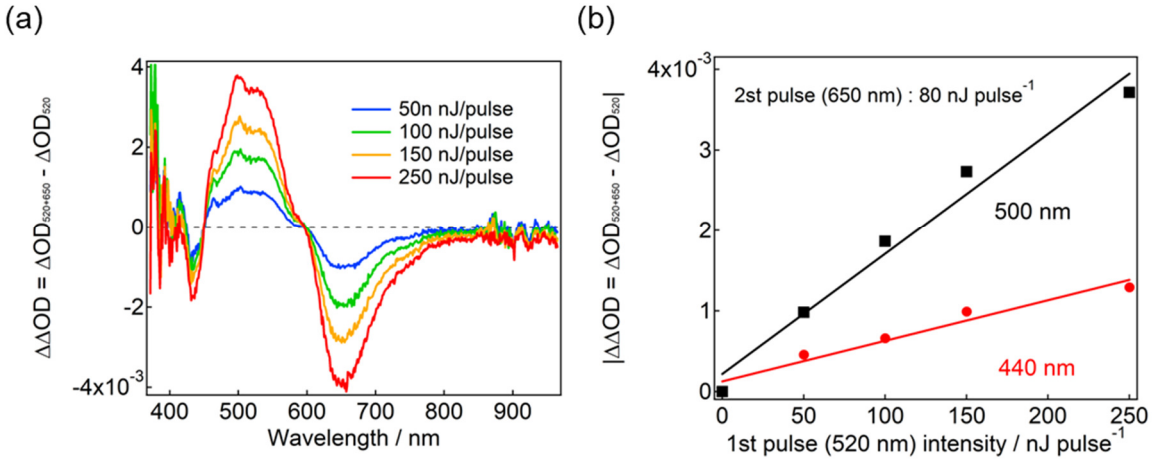

Figure S28. Pump-push ΔΔOD spectra of PMI-CdS in CHCl3 with a pump-push delay of 5 ps. (a) Spectra at a probe delay of 20 ps obtained at different pump-pulse intensities, and (b) plots of the absolute ΔΔOD values at 440 and 500 nm as a function of the pump-pulse energy. The intensity of the 650-nm push pulse was fixed at 80 nJ pulse−1.

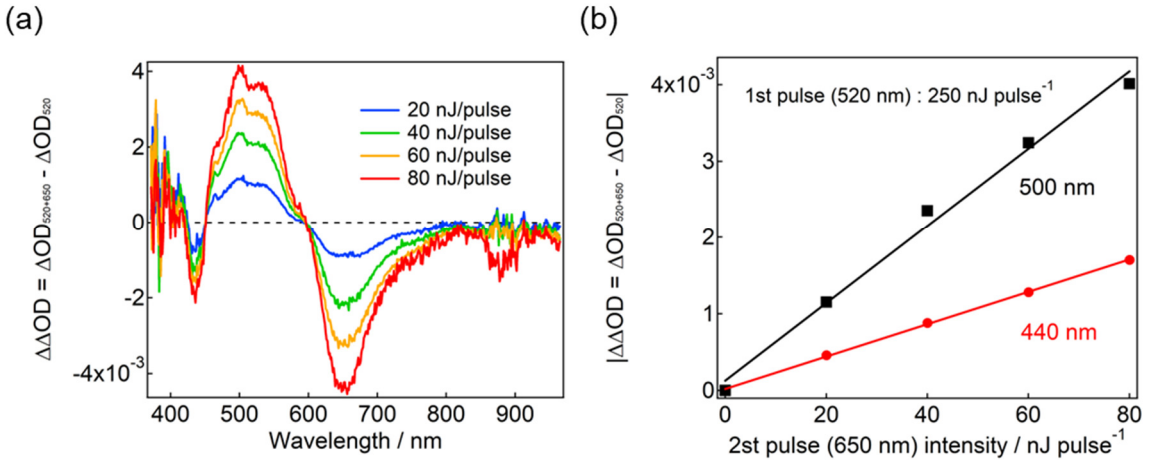

Figure S29. Pump-push ΔΔOD spectra of PMI-CdS in CHCl3 with a pump-push delay of 5 ps. (a) Spectra at a probe delay of 20 ps obtained at different push-pulse intensities, and (b) plots of the absolute ΔΔOD values at 440 and 500 nm as a function of the push-pulse energy. The intensity of the 520-nm pump pulse was fixed at 250 nJ pulse−1.

Time evolution of the transient absorbance changes ΔΔOD(*t*) in pump-push-probe spectroscopy.

We consider the time evolution of the transient absorbance in pump-push-probe spectroscopy for a two-level system consisting of the S_0 and S_1 states. Initially, the molecules are in the S_0 state, and a pump pulse promotes a fraction of them into the S_1 state. After a delay of 5 ps, a push pulse induces stimulated emission from S_1 to S_0, resulting in partial depopulation of the S_1 state. The change in absorbance induced by the pump pulse is given by eq 1.

$$\Delta\mathrm{OD}(t) = (\varepsilon_{\mathrm{S1}} - \varepsilon_{\mathrm{S0}})c_{\mathrm{S1}}(t)l \qquad (1)$$

Here, t is the time delay between the pump and probe pulses, $\varepsilon_{\mathrm{S0}}$ and $\varepsilon_{\mathrm{S1}}$ are the molar absorption coefficients of the S_0 and S_1 states, respectively, $c_{\mathrm{S1}}(t)$ is the concentration of the S_1 state at time *t*, and l is the optical path length of the cell. The time evolution of the S1-state concentration is given by eq 2.

$$c_{\mathrm{S1}}(t) = c_{\mathrm{S1}}(0\ \mathrm{ps})\exp\left(-\frac{t}{\tau_{\mathrm{S1}}}\right) \qquad (2)$$

Here, τ_{S1} is the lifetime of the S_1 state. The absorbance change induced when the push pulse is applied 5 ps after the pump pulse is given by eq 3.

$$\Delta\Delta\mathrm{OD}(t) = \Delta\mathrm{OD}(t)_{\text{push ON}} - \Delta\mathrm{OD}(t)_{\text{push OFF}} \quad (3)$$

$\Delta\mathrm{OD}(t)_{\text{push ON}}$ and $\Delta\mathrm{OD}(t)_{\text{push OFF}}$ correspond to the absorbance changes with and without the push pulse, respectively, and are given by eqs 4 and 5.

$$\Delta\mathrm{OD}(t)_{\text{push ON}} = (\varepsilon_{\mathrm{S1}} - \varepsilon_{\mathrm{S0}})\left(1 - n_{\mathrm{push}}\right)c_{\mathrm{S1}}(5\ \mathrm{ps})\exp\left(-\frac{t'}{\tau_{\mathrm{S1}}}\right)l$$

$$= (\varepsilon_{\mathrm{S1}} - \varepsilon_{\mathrm{S0}})\left(1 - n_{\mathrm{push}}\right)c_{\mathrm{S1}}(0\ \mathrm{ps})\exp\left(-\frac{5\ \mathrm{ps}}{\tau_{\mathrm{S1}}}\right)\exp\left(-\frac{t\prime}{\tau_{\mathrm{S1}}}\right)l \qquad (4)$$

$$\Delta\mathrm{OD}(t)_{\text{push OFF}} = (\varepsilon_{\mathrm{S1}} - \varepsilon_{\mathrm{S0}})c_{\mathrm{S1}}(t)l = (\varepsilon_{\mathrm{S1}} - \varepsilon_{\mathrm{S0}})c_{\mathrm{S1}}(0\ \mathrm{ps})\exp\left(-\frac{5\ \mathrm{ps}}{\tau_{\mathrm{S1}}}\right)\exp\left(-\frac{t\prime}{\tau_{\mathrm{S1}}}\right)l \qquad (5)$$

Here, t' is the time delay between the push and probe pulses, and n_{push} is the deactivation efficiency of the S_1 state molecules induced by the push pulse. The fraction of molecules remaining in the S_1 state is therefore given by $1 - n_{\mathrm{push}}$. The absorbance changes described by eqs 4 and 5 correspond to the blue and red curves, respectively (Figure S30a). Consequently, the transient absorbance is given by eq 6.

$$\Delta\Delta\mathrm{OD}(t) = -(\varepsilon_{\mathrm{S1}} - \varepsilon_{\mathrm{S0}})n_{\mathrm{push}}c_{\mathrm{S1}}(0\ \mathrm{ps})\exp\left(-\frac{5\ \mathrm{ps}}{\tau_{\mathrm{S1}}}\right)\exp\left(-\frac{t\prime}{\tau_{\mathrm{S1}}}\right)l \quad (6)$$

The absorbance change described by eq 6 still contains an exponential term governed by the S_1 state lifetime. Thus, even in a two-level system consisting only of the S_0 and S_1 states, this component can appear when only stimulated emission is induced.

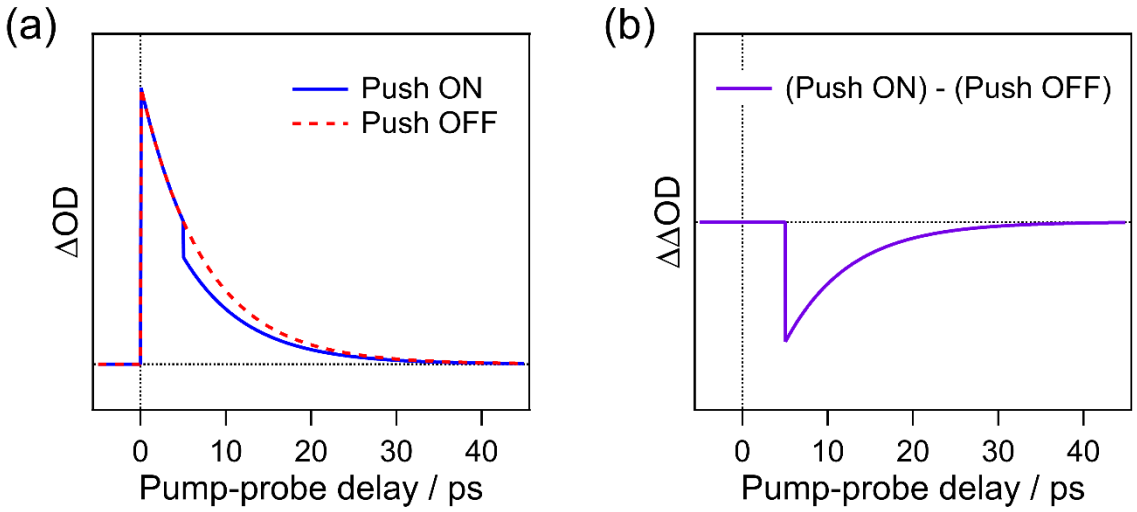

Figure S30. Time evolution of the transient absorption (a) with and without push-pulse irradiation and (b) in the pump-push-probe.

14. DFT calculations

All calculations were carried out using the Gaussian 16 program (Revision C.02).[10] The molecular structure was fully optimized at the B3LYP/6-31+G(d,p) level of theory. Vibrational analysis based on analytical second derivatives was performed to confirm that each stationary point corresponded to a minimum on the potential energy surface. TDDFT calculations were then performed at the same level of theory for the optimized structure.

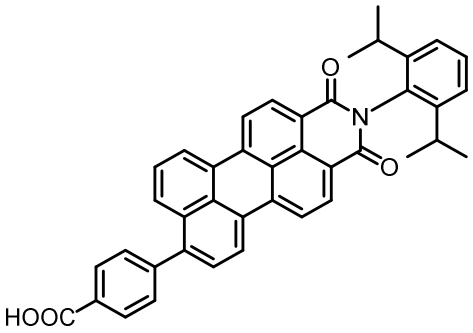

PMI

Table S3. Standard orientation of the optimized geometry of PMI at the B3LYP/6-31+G(d,p) level.

Tag	Symbol	Coordinates (Angstroms)		
		X	Y	Z
1	C	-3.7983250	2.7655480	-1.3971930
2	C	-4.5998200	1.7441020	-0.9352630
3	C	-4.0299120	0.5772110	-0.3596890
4	C	-2.5963590	0.4612700	-0.2979980
5	C	-1.7800230	1.5417910	-0.7717610
6	C	-2.4007490	2.6681980	-1.3064850
7	C	-4.8509700	-0.4969030	0.1211590
8	C	-4.2354640	-1.6481290	0.5864340
9	C	-2.8391300	-1.7654860	0.6332320
10	C	-2.0003930	-0.7351980	0.2184110
11	C	-0.5343490	-0.8494210	0.2924800
12	C	0.2738580	0.2390160	-0.1647970
13	C	-0.3120490	1.4334600	-0.6914870
14	C	1.6997410	0.1311190	-0.0905080
15	C	2.5189760	1.1974860	-0.5347120
16	C	1.9304320	2.3473150	-1.0377920
17	C	0.5378750	2.4606730	-1.1118130
18	C	0.1031130	-1.9860440	0.7985720
19	C	1.4969820	-2.0845130	0.8662110
20	C	2.2995390	-1.0424080	0.4281530
21	C	3.7722280	-1.1704260	0.5200950
22	N	4.5383110	-0.0839500	0.0561730
23	C	3.9955270	1.1018640	-0.4754220
24	C	-6.3378870	-0.4186620	0.1463440
25	O	4.7247520	2.0035660	-0.8693380
26	O	4.3132920	-2.1687130	0.9792580
27	C	5.9901310	-0.1934460	0.1311930

28	C	-7.0093110	0.5900510	0.8626430
29	C	-8.3989070	0.6233850	0.9193000
30	C	-9.1624640	-0.3590570	0.2707180
31	C	-8.5013630	-1.3643300	-0.4496780
32	C	-7.1081340	-1.3926850	-0.5100710
33	C	-10.6556760	-0.2567700	0.3649320
34	O	-11.2328290	0.7671260	0.6506630
35	O	-11.3748640	-1.3848620	0.1112510
36	C	6.6873290	-0.7950550	-0.9408690
37	C	8.0845300	-0.8772060	-0.8388000
38	C	8.7676990	-0.4012000	0.2738990
39	C	8.0529170	0.1792900	1.3148300
40	C	6.6559420	0.3062290	1.2733300
41	C	6.0892580	-1.4276610	-2.2081480
42	C	5.7144190	-2.9094790	-1.9845260
43	C	4.9580610	-0.6714520	-2.9283230
44	C	6.0323290	1.0300120	2.4779550
45	C	5.9050400	2.5492010	2.2286810
46	C	4.7346760	0.4544900	3.0737410
47	H	-4.2451320	3.6501490	-1.8404820
48	H	-5.6765440	1.8221270	-1.0249210
49	H	-1.8082630	3.4945330	-1.6794050
50	H	-4.8457210	-2.4678060	0.9536300
51	H	-2.4248970	-2.6881510	1.0208120
52	H	2.5702560	3.1563620	-1.3736060
53	H	0.1291490	3.3813230	-1.5091350
54	H	-0.4788120	-2.8258420	1.1575550
55	H	1.9706800	-2.9750580	1.2652390
56	H	-6.4335180	1.3425050	1.3926870
57	H	-8.9142740	1.4030750	1.4699370
58	H	-9.0570390	-2.1135670	-1.0086780
59	H	-6.6113190	-2.1641300	-1.0905120
60	H	-10.7976250	-2.1570930	0.0288830
61	H	8.6406990	-1.3310370	-1.6548050
62	H	9.8495960	-0.4820580	0.3294440
63	H	8.5841730	0.5518350	2.1866800
64	H	6.9267070	-1.4316460	-2.9171430
65	H	4.8917610	-3.0184760	-1.2741190
66	H	6.5644750	-3.4739540	-1.5880730
67	H	5.4153080	-3.3654180	-2.9359110
68	H	3.9874960	-0.7975650	-2.4405340
69	H	4.8553810	-1.0730380	-3.9427150
70	H	5.1701670	0.3980430	-3.0075600
71	H	6.7848150	0.9156520	3.2683330
72	H	5.1835490	2.7731940	1.4396500
73	H	6.8647900	2.9789210	1.9243620
74	H	5.5819440	3.0514850	3.1483340
75	H	3.8480290	0.7185110	2.4906560
76	H	4.5896570	0.8747280	4.0753230
77	H	4.7775960	-0.6339490	3.1663220

SCF Done: E(RB3LYP)	=	-1936.90346070 A.U.
Zero-point correction	=	0.613358 (Hartree/Particle)
Thermal correction to Energy	=	0.651130
Thermal correction to Enthalpy	=	0.652075
Thermal correction to Gibbs Free Energy	=	0.541170
Sum of electronic and zero-point Energies	=	-1936.290298
Sum of electronic and thermal Energies	=	-1936.252526
Sum of electronic and thermal Enthalpies	=	-1936.251582
Sum of electronic and thermal Free Energies	=	-1936.362487

Low frequencies --- -2.8483 -0.0008 0.0005 0.0009 0.1088 3.2606

Low frequencies --- 11.7397 15.5771 22.1703

Results of the TDDFT calculations

Excited State 1: Singlet-A 2.4287 eV 510.49 nm f=0.8011 <S**2>=0.000

158 -> 159 0.70519

This state for optimization and/or second-order correction.

Total Energy, E(TD-HF/TD-DFT) = -1936.81440329

Copying the excited state density for this state as the 1-particle RhoCI density.

Excited State 2: Singlet-A 2.7461 eV 451.49 nm f=0.0021 <S**2>=0.000

157 -> 159 0.70456

Excited State 3: Singlet-A 2.9256 eV 423.79 nm f=0.0000 <S**2>=0.000

155 -> 159 0.10684

156 -> 159 0.69340

Excited State 4: Singlet-A 3.2975 eV 375.99 nm f=0.0064 <S**2>=0.000

154 -> 159 0.10969

158 -> 160 0.68693

Excited State 5: Singlet-A 3.3437 eV 370.80 nm f=0.0000 <S**2>=0.000

155 -> 159 0.68015

156 -> 159 -0.11517

Excited State 6: Singlet-A 3.4760 eV 356.69 nm f=0.0036 <S**2>=0.000

152 -> 159 0.22583

153 -> 159 0.53542

154 -> 159 -0.17478
158 -> 162 0.31170

Excited State 7: Singlet-A 3.6014 eV 344.27 nm f=0.0139 <S**2>=0.000
151 -> 159 0.13409
152 -> 159 -0.27693
153 -> 159 0.16975
154 -> 159 0.53497
158 -> 161 0.17261
158 -> 162 0.17481

Excited State 8: Singlet-A 3.6883 eV 336.16 nm f=0.0045 <S**2>=0.000
150 -> 159 0.19707
152 -> 159 0.40238
153 -> 159 -0.22187
154 -> 159 0.18546
158 -> 161 0.42090
158 -> 165 -0.12906

Excited State 9: Singlet-A 3.7244 eV 332.90 nm f=0.0199 <S**2>=0.000
151 -> 159 -0.28247
152 -> 159 -0.33077
154 -> 159 -0.16823
158 -> 161 0.38261
158 -> 162 -0.19671
158 -> 163 0.23613
158 -> 165 0.12874

Excited State 10: Singlet-A 3.7663 eV 329.19 nm f=0.0052 <S**2>=0.000
151 -> 159 0.40965
152 -> 159 -0.11177
153 -> 159 -0.18096
154 -> 159 -0.18851
158 -> 162 0.25227
158 -> 163 0.39742

Excited State 11: Singlet-A 3.7901 eV 327.12 nm f=0.0001 <S**2>=0.000
148 -> 159 -0.11405

149 -> 159 0.66519

Excited State 12: Singlet-A 3.8767 eV 319.82 nm f=0.0339 <S**2>=0.000
150 -> 159 0.49051
151 -> 159 0.23409
153 -> 159 0.25061
158 -> 162 -0.24682
158 -> 164 -0.12187
158 -> 165 -0.21455

Excited State 13: Singlet-A 3.9757 eV 311.86 nm f=0.0006 <S**2>=0.000
146 -> 159 -0.10395
147 -> 159 0.12753
148 -> 159 -0.14992
151 -> 159 -0.16135
152 -> 159 0.13284
154 -> 159 0.24982
158 -> 161 -0.27691
158 -> 162 -0.12432
158 -> 163 0.47779

Excited State 14: Singlet-A 4.0557 eV 305.70 nm f=0.0002 <S**2>=0.000
157 -> 160 0.69381
157 -> 163 -0.12351

Excited State 15: Singlet-A 4.1030 eV 302.18 nm f=0.0050 <S**2>=0.000
148 -> 159 0.47144
150 -> 159 0.28413
151 -> 159 -0.21858
158 -> 161 -0.15027
158 -> 162 0.14833
158 -> 164 0.24696

Excited State 16: Singlet-A 4.1359 eV 299.78 nm f=0.0173 <S**2>=0.000
150 -> 159 -0.16963
151 -> 159 0.22720
152 -> 159 0.12328
158 -> 162 -0.32850

158 -> 164 0.50836

Excited State 17: Singlet-A 4.2145 eV 294.18 nm f=0.0049 <S**2>=0.000
147 -> 159 0.20700
148 -> 159 0.43165
150 -> 159 -0.19584
152 -> 159 0.12494
153 -> 159 0.10388
158 -> 161 0.10183
158 -> 162 -0.19001
158 -> 164 -0.35746

Excited State 18: Singlet-A 4.2800 eV 289.68 nm f=0.0006 <S**2>=0.000
156 -> 160 0.68038
156 -> 163 -0.16510

Excited State 19: Singlet-A 4.2976 eV 288.50 nm f=0.0098 <S**2>=0.000
146 -> 159 -0.13643
147 -> 159 0.62313
148 -> 159 -0.11868
152 -> 159 -0.10638
158 -> 163 -0.14610

Excited State 20: Singlet-A 4.4269 eV 280.07 nm f=0.0008 <S**2>=0.000
146 -> 159 0.60120
146 -> 160 0.18812
147 -> 159 0.12043
147 -> 160 0.14101
148 -> 160 -0.13921
154 -> 160 0.10579
157 -> 161 0.11176

Excited State 21: Singlet-A 4.4323 eV 279.73 nm f=0.0001 <S**2>=0.000
146 -> 159 -0.10319
157 -> 161 0.66332
157 -> 162 -0.12693
157 -> 163 0.14084

Excited State 22: Singlet-A 4.5739 eV 271.07 nm f=0.0001 <S**2>=0.000

157 -> 160 0.12199

157 -> 161 -0.15237

157 -> 163 0.67358

Excited State 23: Singlet-A 4.5998 eV 269.54 nm f=0.0006 <S**2>=0.000

156 -> 161 0.65254

156 -> 162 -0.13713

156 -> 163 0.15199

Excited State 24: Singlet-A 4.6111 eV 268.88 nm f=0.0000 <S**2>=0.000

157 -> 161 0.11138

157 -> 162 0.67864

157 -> 164 0.12591

Excited State 25: Singlet-A 4.6422 eV 267.08 nm f=0.2048 <S**2>=0.000

150 -> 159 0.19914

151 -> 159 0.13349

152 -> 161 -0.10600

153 -> 160 -0.12541

154 -> 160 0.24353

158 -> 165 0.53161

Excited State 26: Singlet-A 4.7200 eV 262.68 nm f=0.0883 <S**2>=0.000

146 -> 159 -0.27142

146 -> 160 0.29496

147 -> 159 -0.11889

147 -> 160 0.21399

148 -> 160 -0.26567

154 -> 160 0.29520

158 -> 165 -0.18715

Excited State 27: Singlet-A 4.7473 eV 261.17 nm f=0.0001 <S**2>=0.000

155 -> 160 -0.26710

155 -> 163 0.18702

156 -> 160 0.16408

156 -> 161 -0.14717

156 -> 163 0.55822

Excited State 28: Singlet-A 4.7983 eV 258.39 nm f=0.0023 <S**2>=0.000

145 -> 159 0.69650

Excited State 29: Singlet-A 4.8224 eV 257.10 nm f=0.0312 <S**2>=0.000

151 -> 160 0.18906

152 -> 160 0.31199

153 -> 160 0.51790

154 -> 162 -0.13209

156 -> 162 -0.14782

158 -> 165 0.12539

Excited State 30: Singlet-A 4.8273 eV 256.84 nm f=0.0012 <S**2>=0.000

153 -> 160 0.11037

155 -> 160 0.12586

156 -> 162 0.62981

156 -> 163 0.13911

156 -> 164 0.13180

156 -> 165 0.10432

Excited State 31: Singlet-A 4.8327 eV 256.55 nm f=0.0011 <S**2>=0.000

155 -> 160 0.51673

155 -> 163 -0.24696

156 -> 162 -0.16679

156 -> 163 0.31370

Excited State 32: Singlet-A 4.9050 eV 252.77 nm f=0.0074 <S**2>=0.000

154 -> 160 0.10171

158 -> 166 0.63831

158 -> 168 -0.25679

Excited State 33: Singlet-A 4.9094 eV 252.54 nm f=0.2879 <S**2>=0.000

146 -> 160 -0.14328

147 -> 160 -0.12357

148 -> 160 0.29050

154 -> 160 0.53559

154 -> 162 0.10069

158 -> 165 -0.10122

158 -> 166 -0.11713

Excited State 34: Singlet-A 4.9483 eV 250.56 nm f=0.0306 <S**2>=0.000
147 -> 160 -0.20240
148 -> 160 -0.12316
151 -> 160 0.18458
153 -> 160 -0.10373
154 -> 164 0.12716
157 -> 162 -0.10590
157 -> 164 0.56480

Excited State 35: Singlet-A 4.9597 eV 249.98 nm f=0.0548 <S**2>=0.000
146 -> 160 0.10372
147 -> 160 0.27881
148 -> 160 0.20011
151 -> 160 -0.31419
153 -> 160 0.15594
154 -> 164 -0.18191
157 -> 164 0.37875

Excited State 36: Singlet-A 4.9966 eV 248.14 nm f=0.0029 <S**2>=0.000
143 -> 159 -0.14679
149 -> 161 0.12059
150 -> 160 0.14692
152 -> 160 0.30576
153 -> 160 -0.18884
155 -> 161 0.47499
155 -> 162 -0.10588

Excited State 37: Singlet-A 4.9983 eV 248.05 nm f=0.0095 <S**2>=0.000
143 -> 159 0.11421
150 -> 160 0.20082
152 -> 160 0.42727
153 -> 160 -0.25386
153 -> 163 0.11325
155 -> 161 -0.33845

Excited State 38: Singlet-A 5.0466 eV 245.68 nm f=0.0287 <S**2>=0.000

147 -> 160 0.21725
148 -> 160 0.26043
151 -> 160 0.49325
151 -> 163 -0.10544
154 -> 161 0.21465

Excited State 39: Singlet-A 5.0718 eV 244.46 nm f=0.0012 <S**2>=0.000
143 -> 159 -0.13006
144 -> 159 0.67906

Excited State 40: Singlet-A 5.0845 eV 243.85 nm f=0.0000 <S**2>=0.000
143 -> 159 0.65383
144 -> 159 0.12545
155 -> 161 0.18672

Excited State 41: Singlet-A 5.1169 eV 242.30 nm f=0.0058 <S**2>=0.000
158 -> 166 0.25378
158 -> 167 -0.10711
158 -> 168 0.62407

Excited State 42: Singlet-A 5.1376 eV 241.33 nm f=0.0085 <S**2>=0.000
156 -> 169 -0.36185
157 -> 167 0.45475
158 -> 167 0.36124

Excited State 43: Singlet-A 5.1777 eV 239.46 nm f=0.0054 <S**2>=0.000
137 -> 159 -0.11092
150 -> 160 0.14712
150 -> 161 -0.10878
151 -> 162 0.16918
152 -> 162 -0.11565
153 -> 160 0.13902
153 -> 161 0.41287
153 -> 163 0.13324
154 -> 162 0.16112
158 -> 167 0.13610
158 -> 171 -0.20654
158 -> 172 -0.10791

Excited State 44: Singlet-A 5.1887 eV 238.95 nm f=0.0004 <S**2>=0.000

156 -> 162 -0.14497

156 -> 164 0.61472

156 -> 165 0.12393

158 -> 167 0.20075

Excited State 45: Singlet-A 5.1904 eV 238.87 nm f=0.0036 <S**2>=0.000

156 -> 164 -0.24961

156 -> 169 0.19111

157 -> 167 -0.25976

158 -> 167 0.49112

158 -> 170 0.19780

Excited State 46: Singlet-A 5.2130 eV 237.84 nm f=0.0003 <S**2>=0.000

149 -> 160 0.30180

149 -> 163 -0.22078

155 -> 160 0.33027

155 -> 163 0.43234

Excited State 47: Singlet-A 5.2275 eV 237.18 nm f=0.0001 <S**2>=0.000

157 -> 164 -0.11889

157 -> 165 0.67322

Excited State 48: Singlet-A 5.2379 eV 236.71 nm f=0.0142 <S**2>=0.000

150 -> 160 0.47828

150 -> 163 -0.11675

151 -> 160 0.13248

152 -> 160 -0.23753

153 -> 161 -0.16697

154 -> 162 0.14567

157 -> 165 0.13758

158 -> 169 0.12349

158 -> 171 0.17431

Excited State 49: Singlet-A 5.2629 eV 235.58 nm f=0.0398 <S**2>=0.000

137 -> 159 -0.10334

138 -> 159 0.18729

142 -> 159 -0.13868
150 -> 160 0.12844
152 -> 163 0.10462
153 -> 161 -0.14698
153 -> 163 0.13519
154 -> 161 0.27090
154 -> 162 0.11067
158 -> 169 -0.10134
158 -> 170 0.25600
158 -> 171 -0.21551
158 -> 172 0.28654

Excited State 50: Singlet-A 5.2662 eV 235.43 nm f=0.0048 <S**2>=0.000
153 -> 161 0.16647
158 -> 167 -0.19432
158 -> 169 0.17780
158 -> 170 0.57956
158 -> 171 0.10903

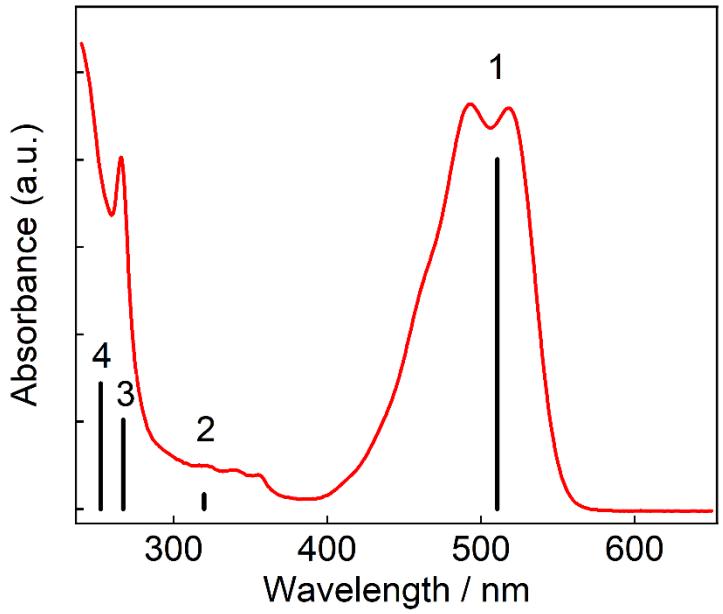

Figure S31. UV-vis absorption spectrum of PMI in $CHCl_3$ at room temperature. The calculated absorption spectrum at the B3LYP/6-31+G(d,p) level of theory is shown as black vertical bars.

Table S4. Selected calculated electronic transitions of PMI at the B3LYP/6-31+G(d,p) level.

No.	Wavelength (nm)	coefficients	Electronic Transition	*f*
1	510.49	0.70018	158 HOMO →159 LUMO	0.8011
2	319.82	0.49051	150 HOMO−8 →159 LUMO	0.0339
		0.23409	151 HOMO−7 →159 LUMO	
		0.25061	153 HOMO−5 →159 LUMO	
		-0.24682	158 HOMO →162 LUMO+3	
		-0.12187	158 HOMO →164 LUMO+5	
		-0.21455	158 HOMO →165 LUMO+6	
3	267.08	0.19914	150 HOMO−8 →159 LUMO	0.2048
		0.13349	151 HOMO−7 →159 LUMO	
		-0.106	152 HOMO−6 →161 LUMO+2	
		-0.12541	153 HOMO−5 →160 LUMO+1	
		0.24353	154 HOMO−4 →160 LUMO+1	
		0.53161	158 HOMO →165 LUMO+6	
4	252.54	-0.14328	146 HOMO−12 →160 LUMO+1	0.2879
		-0.12357	147 HOMO−11 →160 LUMO+1	
		0.2905	148 HOMO−10 →160 LUMO+1	
		0.53559	154 HOMO−4 →160 LUMO+1	
		0.10069	154 HOMO−4 →162 LUMO+3	
		-0.10122	158 HOMO →165 LUMO+6	
		-0.11713	158 HOMO →166 LUMO+7	

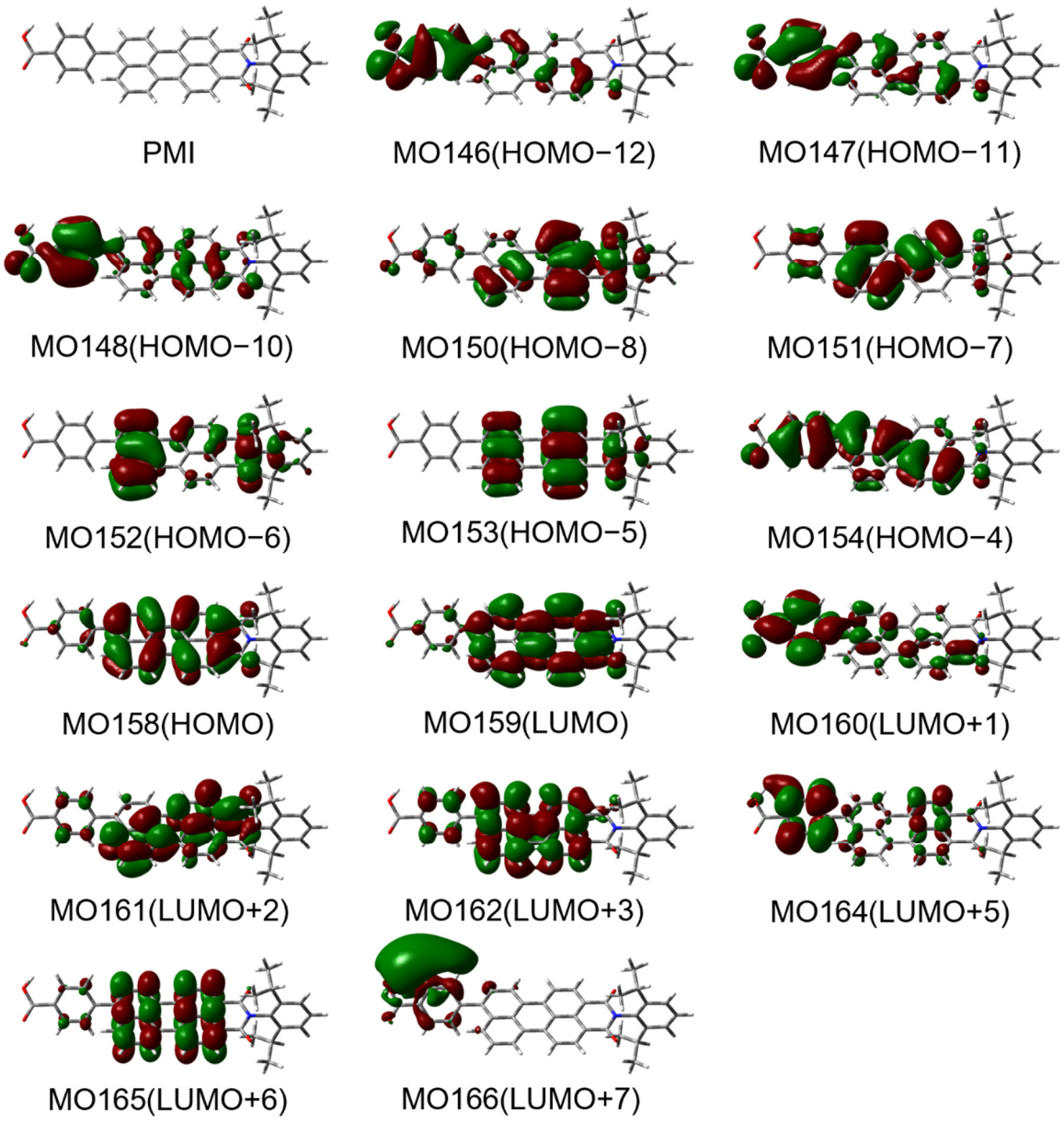

Figure S32. The relevant molecular orbitals of PMI calculated at the B3LYP/6-31+G(d,p) level of theory.

15. References

(1) Usui, R.; Yamamoto, K.; Okajima, H.; Mutoh, K.; Sakamoto, A.; Abe, J.; Kobayashi, Y. Photochromic Radical Complexes That Show Heterolytic Bond Dissociation. *J. Am. Chem. Soc.* **2020**, *142*, 10132–10142.

(2) Chen, X.; Wang, Y. N.; Rong, R. X.; Zhao, C. M.; Li, X. L.; Wang, K. R. Synthesis, Thermo-Responsive Behavior of Cyclodextrin Modified Bi-Perylene Monoimide Derivative. *Dyes Pigm.* **2019**, *160*, 779–786.

(3) Cheriya, R. T.; Mallia, A. R.; Hariharan, M. Light Harvesting Vesicular Donor-Acceptor Scaffold Limits the Rate of Charge Recombination in the Presence of an Electron Donor. *Energy Environ. Sci*. **2014**, *7*, 1661–1669.

(4) Navarro, J. R. G.; Plugge, M.; Loumaigne, M.; Sanchez-Gonzalez, A.; Mennucci, B.; Débarre, A.; Brouwer, A. M.; Werts, M. H. V. Probing the Interactions between Disulfide-Based Ligands and Gold Nanoparticles Using a Functionalised Fluorescent Perylene-Monoimide Dye. Photochem. *Photobiol. Sci*. **2010**, *9*, 1042–1054.

(5) Li, Z.; Ji, Y.; Xie, R.; Grisham, S. Y.; Peng, X. Correlation of CdS Nanocrystal Formation with Elemental Sulfur Activation and Its Implication in Synthetic Development. *J. Am. Chem. Soc.* **2011**, *133*, 17248–17256.

(6) Kimura, M.; Yoshioka, D.; Chang, I. Y.; Irizawa, A.; Shibata, D.; Imada, S.; Kobayashi, Y. Photochromic Color Tuning of Copper-Doped Zinc Sulfide Nanocrystals by Control of Local Dopant Environments. *Angew. Chem. Int. Ed*. **2025**, *64*.

(7) Gosztola, D.; Niemczyk, M. P.; Svec, W.; Lukas, A. S.; Wasielewski, M. R. Excited Doublet States of Electrochemically Generated Aromatic Imide and Diimide Radical Anions. *J. Phys. Chem. A* **2000**, *104*, 6545–6551.

(8) De Roo, J. The Surface Chemistry of Colloidal Nanocrystals Capped by Organic Ligands. *Chem. Mater.* **2023**, *35*, 3781–3792.

(9) H. Kisch, Semiconductor Photocatalysis Principles and Applications, *Wiley, Weinheim*, **2015**.

(10) Frisch, M. J.; Trucks, G. W.; Schlegel, H. B.; Scuseria, G. E.; Robb, M. A.; Cheeseman, J. R.; Scalmani, G.; Barone, V.; Petersson, G. A.; Nakatsuji, H.; Li, X.; Caricato, M.; Marenich, A. V.; Bloino, J.; Janesko, B. G.; Gomperts, R.; Mennucci, B.; Hratchian, H. P.; Ortiz, J. V.; Izmaylov, A. F.; Sonnenberg, J. L.; Williams-Young, D.; Ding, F.; Lipparini, F.; Egidi, F.; Goings, J.; Peng, B.; Petrone, A.; Henderson, T.; Ranasinghe, D.; Zakrzewski, V. G.; Gao, J.; Rega, N.; Zheng, G.; Liang, W.; Hada, M.; Ehara, M.; Toyota, K.; Fukuda, R.; Hasegawa, J.; Ishida, M.; Nakajima, T.; Honda, Y.; Kitao, O.; Nakai, H.; Vreven, T.; Throssell, K.; Montgomery, J. A. , Jr.; Peralta, J. E.; Ogliaro, F.; Bearpark, M. J.; Heyd, J. J.; Brothers, E. N.; Kudin, K. N.; Staroverov, V. N.; Keith, T. A.; Kobayashi, R.; Normand, J.; Raghavachari, K.; Rendell, A. P.; Burant, J. C.; Iyengar, S. S.; Tomasi, J.; Cossi, M.; Millam, J. M.; Klene, M.; Adamo, C.; Cammi, R.; Ochterski, J. W.; Martin, R. L.; Morokuma, K.; Farkas, O.; Foresman, J. B.; Fox, D. J. Gaussian 16. Gaussian, Inc.: Wallingford CT **2016**.